Article

A Novel Approach for High-Precision Evaluation of Sphericity Errors Using Computational Geometric Method and Differential Evolution Algorithm

Dongfang Zhao [1,2] , **Junning Cui** [1,2,]* , **Zhisheng Wang** [1,2] and **Yanxu Sun** [1,2]

[1] Center of Ultra-precision Optoelectronic Instrument engineering, Harbin Institute of Technology, Harbin 150080, China; 20b901006@stu.hit.edu.cn (D.Z.); 21b901035@stu.hit.edu.cn (Z.W.); 22b901030@stu.hit.edu.cn (Y.S.)

[2] Key Lab of Ultra-precision Intelligent Instrumentation (Harbin Institute of Technology), Ministry of Industry and Information Technology, Harbin 150080, China

* Correspondence: cuijunning@126.com; Tel.: +86-0451-86412041-803

Abstract: The sphericity error is a critical form and position tolerance for spheres. We explored the distribution of sphericity errors within the solution space to achieve a high-precision evaluation using the minimum zone criteria. Within local solution spaces, we propose treating the evaluation of sphericity errors as a unimodal function optimization task. And computational geometric methods are employed to achieve highly accurate solutions within the local solution spaces. Subsequently, we integrated the computational geometric method with the differential evolution algorithm (DE algorithm). By centering on individual population members of the DE algorithm, we partitioned the local solution spaces and utilized the best solutions within them to optimize the population. With the gradual convergence of the DE algorithm, we successfully achieved the high-precision resolution of sphericity errors. The experimental results demonstrate a significant order-of-magnitude improvement in precision compared to traditional algorithms in the field of sphericity error evaluation, with uncertainty levels reaching magnitudes of 10^{-14} mm. Moreover, this method enhances the accuracy of sphericity error evaluation by approximately 10% for three-coordinate measuring machines. Additionally, we conducted ablation experiments to validate the effectiveness of the proposed computational geometric method. In summary, this approach enables the high-precision evaluation of sphericity errors and provides a practical methodology for applying ultra-precision spheres in precision engineering.

Keywords: high precision; sphericity error; minimum zone criteria; computational geometric method; differential evolution algorithm

1. Introduction

The high-precision sphere constitutes a pivotal component within the realm of precision instruments. A sphere's primary form tolerance characteristic manifests as a sphericity error. This inherent sphericity error, in turn, introduces unwelcome vibrations and noise, directly exerting a tangible influence on these precision instruments' precision and service longevity [1,2]. The measurement and evaluation of the sphericity error are primarily conducted using three-coordinate measuring machines (CMMs) [3,4]. This advanced technology enables the acquisition of extensive contour data for the spheres under examination, which are then meticulously stored in the XYZ coordinate format, forming a substantial dataset [5]. It is crucial to underscore that this dataset's precise and efficient processing stands as a critical imperative for the accurate evaluation of the sphericity error in spherical objects.

According to the standards set by the American Society of Mechanical Engineers (ASME) and the International Organization for Standardization (ISO) [6,7], the processing

of datasets can be executed by applying four distinct criteria: the least squares criterion, the minimum circumscribed criterion, the maximum inscribed criterion, and the minimum zone criterion. The minimum zone criterion is the general default criterion for evaluating the sphericity error [8–10]. The aforementioned criterion enables the acquisition of a unique minimum sphericity error, and it is also the arbitration method when there is inconsistency in the evaluation of the sphericity error. The minimum zone criterion is an unconstrained and non-differentiable optimization problem, which poses significant challenges in terms of finding a viable solution [11–13].

Although the ASME and ISO standards stipulate that the evaluation of sampling point determination should be based on the minimum zone criterion, these standards do not provide a specific computational method for evaluating the spherical error based on the minimum zone criterion. Therefore, the development of a highly accurate and robust method for evaluating sphericity errors is of utmost urgency. Many scholars have extensively examined this issue by presenting a range of computational geometric methods [8,14–18], region search techniques [19], heuristic algorithms [20–22], multi-objecitve optimization methods [23–25], and bio-inspired intelligent optimization algorithms [26–30] to address the problem.

Among these approaches, region search methods are subject to inherent limitations that hinder their ability to accurately determine solutions for sphericity errors. Computational geometric methods for sampling point filtration exhibit enhanced search efficiency and improved results when dealing with fewer sampling points. Nevertheless, as the number of sampling points increases, the search cost escalates rapidly, resulting in unpredictable and fluctuating results. Heuristic algorithms are prone to being influenced by local optima and often struggle to converge effectively. Bio-inspired intelligent optimization algorithms yield more accurate results. However, they involve complex computations and numerous parameters that require optimization. Moreover, a sphericity error assessment, which is carried out to determine the optimal sphere center, minimizing the radius difference of concentric spheres that encompass the sampled contour, is fundamentally a single-objective optimization problem. Despite the potential advantages of applying multi-objective optimization methods to this evaluation, there is a paucity of scholars incorporating them into sphericity error assessment.

To address the problem of inadequate precision in sphericity error evaluation methods, we conducted an in-depth examination of the spatial distribution characteristics of sphericity errors. Based on our research, it is recommended to approach the issue of sphericity errors in the local solution space by treating it as a problem of optimizing a unimodal function. By utilizing computational geometric techniques, it is possible to achieve highly accurate solutions within the confines of the local solution space. Subsequently, by leveraging the advantages of heuristic algorithms for global space exploration, we successfully achieved a high-precision evaluation of sphericity errors. This method presents a novel research avenue for sphericity error evaluation methodologies.

2. Methods

2.1. Mathematical Model of the Minimum Zone Sphericity Error

According to the definitions of the minimum zone spherical error in ASME and ISO, for a given set of sampled contour points, if all data points fall within two concentric spheres, the difference in the radii of these two spheres is referred to as the minimum zone spherical error. Therefore, when evaluating spherical error based on the minimum zone criterion, the central task is to find an ideal sphere center $\mathbf{p}_0^*$ that minimizes the difference in radii between the two concentric spheres (where the radius difference represents the sphericity error, denoted as e) [27,28,31–33]. This task is expressed by Equation (1).

$$e = \min_{\mathbf{P}_0 \in Q} \left\{ \max_{i \in [1,n]} \|\mathbf{p}_i - \mathbf{p}_0\|_2 - \min_{i \in [1,n]} \|\mathbf{p}_i - \mathbf{p}_0\|_2 \right\} \qquad (1)$$

In the equation, *e* represents the spherical error, where $\mathbf{p}_i \in \mathbb{R}^d$, $i = 1, 2, \ldots; n$ denotes the measurement points in a *d*-dimensional space; and $\mathbf{p}_0$ is the center of the concentric sphere. *Q* is a cubic region containing the globally optimal solution, which we call the global solution space.

Figure 1 illustrates the spatial geometric structure of spherical error evaluation based on the minimum zone criterion and the various parameters involved. The construction of the global solution space *Q* requires the computation of the least squares sphere center and the least squares spherical error based on the least square criterion. Subsequently, a cube with a side length equal to the least squares spherical error is constructed around the least squares sphere center, allowing us to infer that the ideal sphere center must lie within this search region.
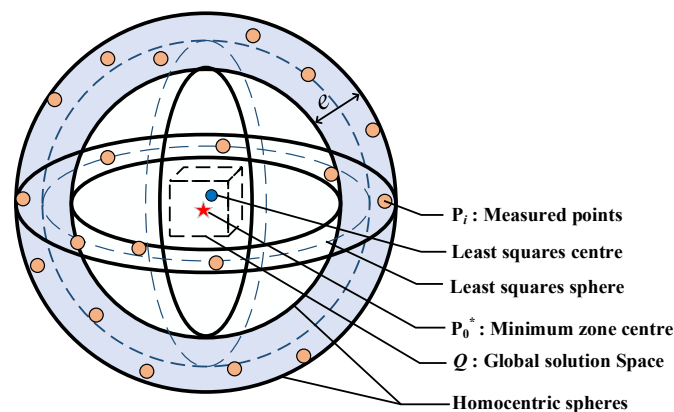

Figure 1. Geometric structure of sphericity error evaluation based on the minimum zone criterion.

2.2. Sphericity Error Spatial Distribution Characteristics

From Equation (1) and Figure 1, it can be observed that the problem of evaluating the sphericity error based on the minimum zone criterion is non-differentiable and unconstrained. Finding an ideal sphere center $\mathbf{p}_0^*$ within three-dimensional space, such that the difference in the radii is minimized when the concentric spheres encompass the spherical contour, poses a highly challenging problem. Meanwhile, existing studies suggest that the ideal sphere center $\mathbf{p}_0^*$ is not unique [10,21]. There are several local optimal solutions near the optimal solution of the sphericity error, and the sphericity error decreases rapidly with a large gradient at the location far from the optimal solution [21].

Therefore, we have undertaken a study on the spatial distribution characteristics of spherical error. We conducted an analysis of the data sourced from reference [15]. Subsequently, we performed 27,000 samplings from the global solution space, calculating the spherical errors for each sampled point. Figure 2a illustrates the distribution of these sampled points, with the color gradient representing the magnitudes of the associated spherical error values. Following this, within this array of 27,000 points, we scrutinized the variations in spherical error values along the directions parallel to the XYZ axes. This scrutiny was carried out with the center O_{LS} (X, Y, Z) of the least squares sphere as the central point, independently assessing the variations along each axis.

Meanwhile, Figure 2b–d show the trend of the sphericity error near the center O_{LS} (X, Y, Z) of the least squares sphere, where the three lines passing through O_{LS} and running parallel to the X-axis, Y-axis, and Z-axis, respectively, are constructed. It is clearly discernible from Figure 2b–d that, at positions considerably distant from the ideal solution, there is a significant gradient in the variation of the spherical error. Conversely, as the position approaches the ideal solution, the evolution of the spherical error gradually becomes more intricate.
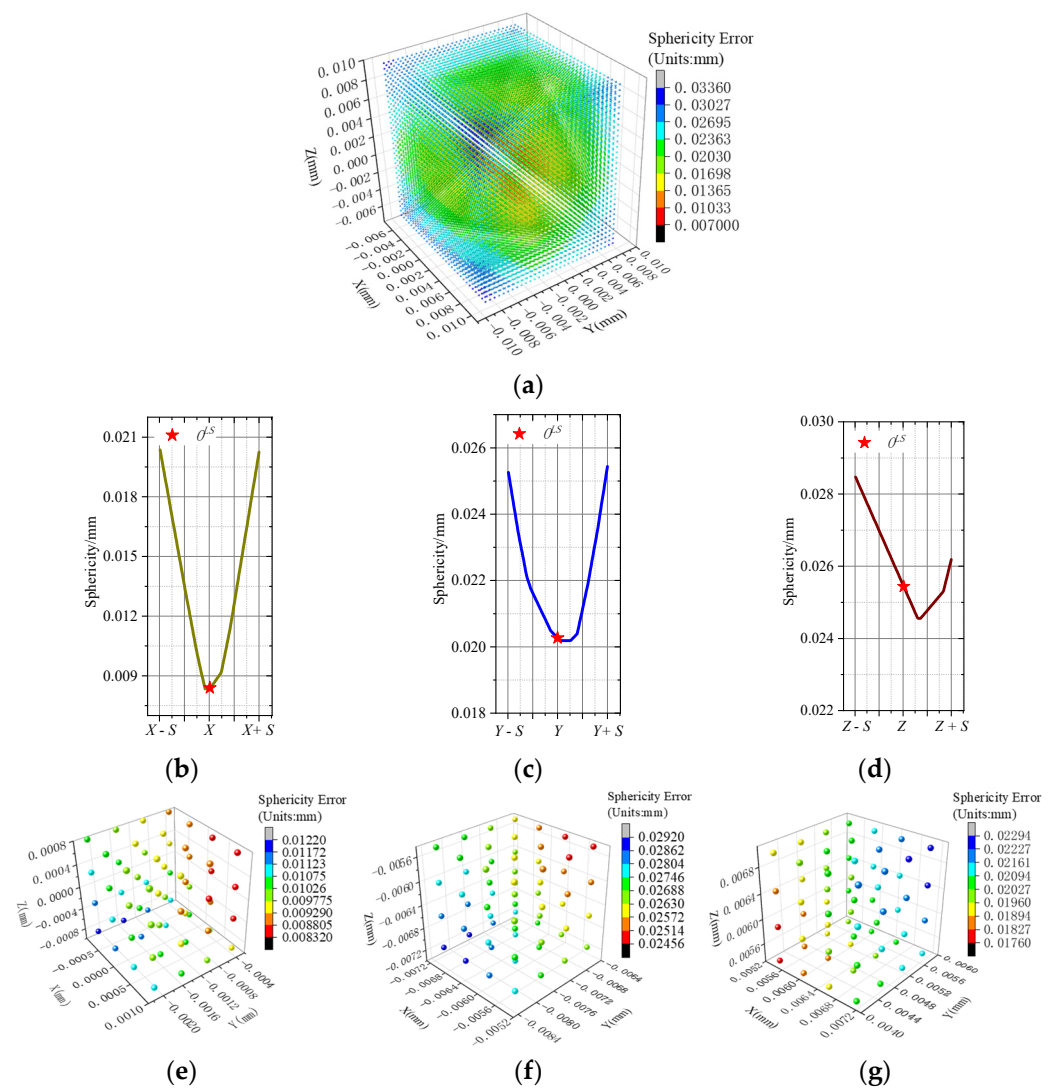
Figure 2. Schematic representation of spherical error distribution characteristics. (**a**) Spherical error distribution of sampling points in the global space; (**b**) change in sphericity along the X-axis; (**c**) change in sphericity along the Y-axis; (**d**) change in sphericity along the Z-axis; (**e**) schematic distribution of sampling points in Local Space A; (**f**) schematic distribution of sampling points in Local Space B; (**g**) schematic distribution of sampling points in Local Space C.

Subsequently, we arbitrarily elected several localized solution spaces from the global solution space, analyzing the spherical error variation of the sampling points within these specific solution spaces. Figure 2e–g illustrate the distribution of sampling points within these localized solution spaces. It can be observed from Figure 2e–g that within smaller regions, the variation of the spherical error manifests a relatively uncomplicated nature, approximating the characteristics of a unimodal function. If the global solution space is divided into different size subregions, then each subregion can be approximated as a single-peaked function for processing. In local spatial domains, unimodal functions can be effectively solved using computational geometry methods, yielding high-precision results.

The algorithm presented in this paper primarily leverages the characteristics of spherical error gradient variations and the approximate unimodal nature of spherical error changes within local spaces for its design. This is the foundation of the local enhancement principle in this paper.

2.3. Principle of the Proposed Method

As demonstrated in Section 2, a comprehensive investigation was carried out to analyze the spatial distribution characteristics of the sphericity error. Given the non-uniqueness of the ideal solution $\mathbf{p}_0^*$ and the potential existence of local optima, the high-precision sphericity error evaluation directly from the global solution space presents a considerable challenge. However, through the adept partitioning of the global solution space into multiple local solutions, it becomes possible to approach the evaluation of the sphericity error as a unimodal function optimization problem within each local space. By employing computational geometry techniques, it is possible to attain high-precision solutions within the confines of these local solution spaces.

Subsequently, the integration of the computational geometry method employed with the DE algorithm is performed. We establish the positions of local solution spaces by utilizing the individuals that are present in the population of differential evolution. During each iteration, the sizes of the local solution spaces are adaptively adjusted based on the distances between the individuals in the population and the global optimum. Additionally, incorporating Lévy flights and simulated annealing techniques allows for the perturbation of the positions of individuals within the population, thereby augmenting the diversity of local solution spaces. After attaining high-precision solutions within the designated local spaces, the DE algorithm individuals are relocated to their respective optimal positions within these local solution spaces. With each successive iteration of the DE algorithm, the population progressively approaches convergence towards the global optimum. As a result, an optimal solution for minimizing the sphericity error is eventually obtained. The overall algorithmic process is depicted in Figure 3. We denote the computational geometric method integrated with the DE algorithm as "Adaptive Local Enhancement". The detailed steps of this approach are outlined in Section 3.2.
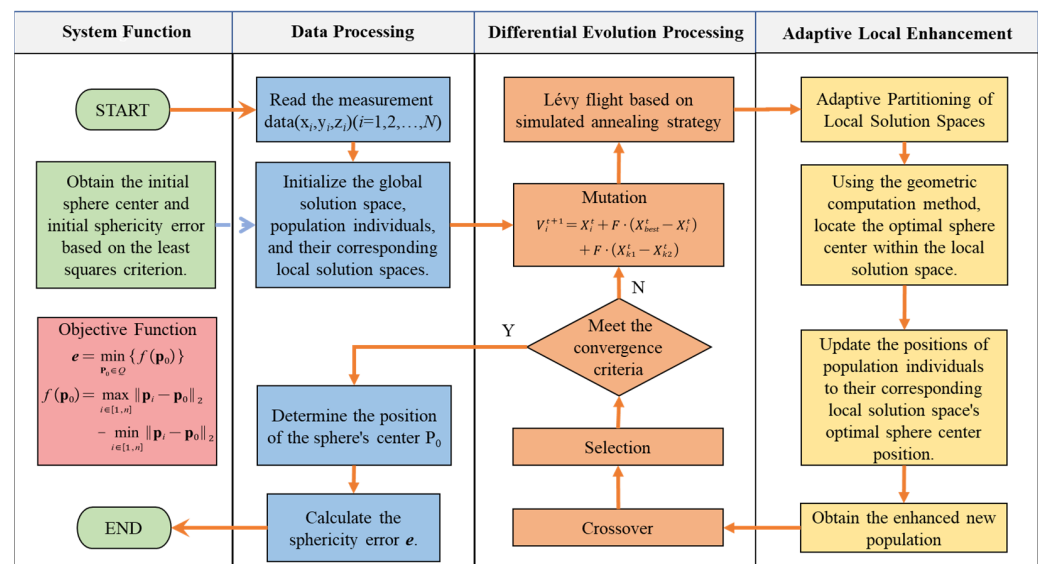
Figure 3. Flowchart of the algorithm.

2.4. Adaptive Local Enhancement Method

2.4.1. Adaptive Partitioning of Local Solution Spaces

Considering the gradually complex variations in the sphericity error when the candidate sphere center approaches the ideal sphere center $\mathbf{p}_0^*$, we devised an adaptive method for partitioning the local solution space. By leveraging the individuals of differential evolution, this method divides the neighborhood of the population into local solution spaces of varying sizes.

During each iteration of the DE algorithm, we calculate the distance denoted as d_i, $i = 1, 2, \ldots, n$ between an individual's optimal solution and the population. The deter-

mination of the distance is contingent upon the expression $d_i = d_i / \max(d_i)$. Subsequently, we determine the size of the individual's neighborhood space according to $L_i = K \cdot d_i + eps$. Here, K is a scaling factor, and eps is a constant that prevents L from becoming zero. The neighborhood search range for each individual, represented as (x_i, y_i, z_i), falls within the interval of $[x_i - L_i, x_i + L_i]$, $[y_i - L_i, y_i + L_i]$ and $[z_i - L_i, z_i + L_i]$. Figure 4 shows the sizes and distributions of these local solution spaces.
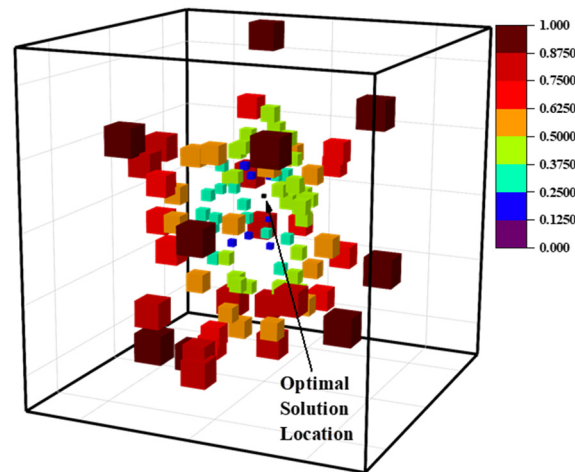
Figure 4. Local solution spaces' sizes and distribution.

2.4.2. Computational Geometric Method for Local Solution Spaces

Once the local solution spaces are determined based on the positions of population individuals, a precise solution need to be conducted for each local solution space. Since we regard the problem of solving the spherical deviation error under the constraint of local solution space as a unimodal function problem, we employ the computational geometry approach shown below.

In the three-dimensional space, the local enhancement process of individuals is shown in Figure 5. According to the predetermined search interval, the initial Z-directional search interval is determined as $\left[Z_L^i = z_i - L_i, Z_R^i = z_i + L_i\right]$, and then the search is performed on two planes Z_1^i, Z_2^i, where $Z_1^i = (Z_R^i + 2Z_L^i)/3, Z_2^i = (2Z_R^i + Z_L^i)/3$. The initial search interval in the Y direction is $\left[Y_L^i = y_i - L_i, Y_R^i = y_i + L_i\right]$ on two planes Z_1^i, Z_2^i, and a search for the local optimal solution in the one-dimensional direction, $Y_1^i = (Y_R^i + 2Y_L^i)/3$ and $Y_1^i = (Y_R^i + 2Y_L^i)/3$, is performed on both planes. Shrinking the search interval according to strategy 1, four positions, $_{Y_1 Z_1} X_{\text{best}}, {}_{Y_2 Z_1} X_{\text{best}}, {}_{Y_2 Z_1} X_{\text{best}}$, and $_{Y_2 Z_2} X_{\text{best}}$, of the local optimal solution can be obtained when satisfying the following condition: $X_R - X_L < 1 \times 10^{-n}$. The local optimal solutions on the Z_1^i, Z_2^i planes are compared, respectively, and the search interval in the Y-direction on the two planes, Z_1^i, Z_2^i, is shrunken according to strategy 2. After satisfying the condition $Y_R - Y_L < 1 \times 10^{-n}$, the optimal solutions $f(X, Y, Z_1^i)$ and $f(X, Y, Z_2^i)$ on the Z_1^i, Z_2^i planes are obtained. Afterward, the Z-directional search space is shrunken according to strategy 3. While satisfying $Z_R - Z_L < 1 \times 10^{-n}$, the local optimal solution is obtained.

$$
\text{Strategy 1}: \begin{cases} X_L^i = X_1^{i-1}, if : f(X_1^{i-1}, Y, Z) > f(X_2^{i-1}, Y, Z) \\ X_R^i = X_2^{i-1}, else \end{cases}
$$

$$
\text{Strategy 2}: \begin{cases} Y_L^i = Y_1^{i-1}, if : f(_{Y_1 Z} X_{\text{best}}, Y_1^{i-1}, Z) > f(_{Y_2 Z} X_{\text{best}}, Y_2^{i-1}, Z) \\ Y_R^i = Y_2^{i-1}, else \end{cases}
$$

$$
\text{Strategy 3}: \begin{cases} Z_L^i = Z_1^{i-1}, if : f(Z_{best}, Y_{best}, Z_1^{i-1}) > f(X_{\text{best}}, Y_{best}, Z_2^{i-1}) \\ Z_R^i = Z_2^{i-1}, else \end{cases}
$$
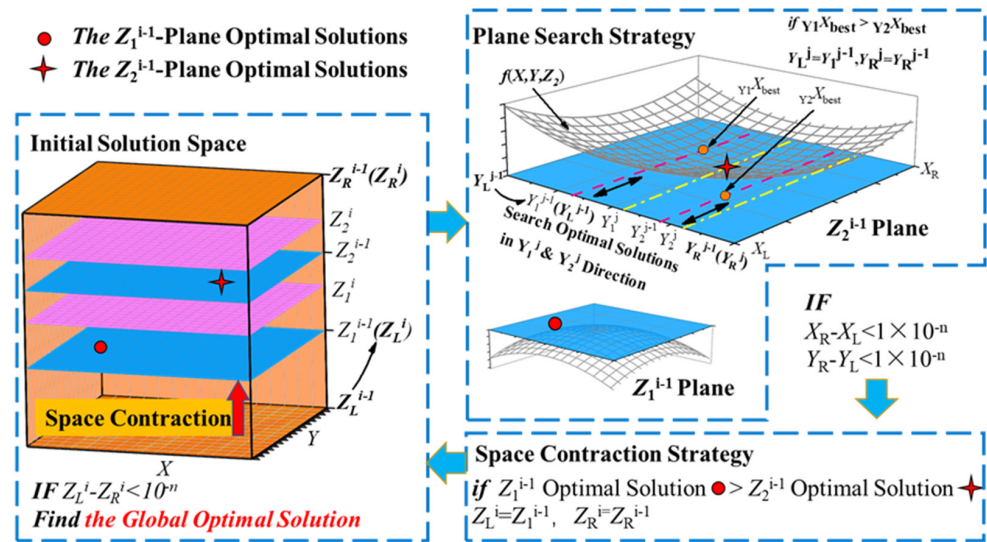
Figure 5. Schematic representation of the computational geometric method for local solution spaces.

Furthermore, for the one-dimensional search area corresponding to Y_1^i on the Z_1^i plane in Figure 5, the detailed search process is illustrated in Figure 6. The middle points, $X_1^{i-1} = (X_R^{i-1} + 2X_L^{i-1})/3$ and $X_2^{i-1} = (2X_R^{i-1} + X_L^{i-1})/3$, are determined based on the neighborhood searching range of the individuals, $\left[X_L^{i-1} = x_{i-1} - L_{i-1}, X_R^{i-1} = x_{i-1} + L_{i-1} \right]$, after which the magnitudes of $f(X_1^{i-1})$ and $f(X_2^{i-1})$ are compared. If $f(X_1^{i-1}) > f(X_2^{i-1})$, then set $X_L^i = X_1^{i-1}$; otherwise, set $X_R^i = X_2^{i-1}$. Through the strategy above, used to shrink the search interval, the optimal solution is considered as the sphericity error at the X_R^i position when $X_R^i - X_L^i < 1 \times 10^{-n}$ is satisfied.
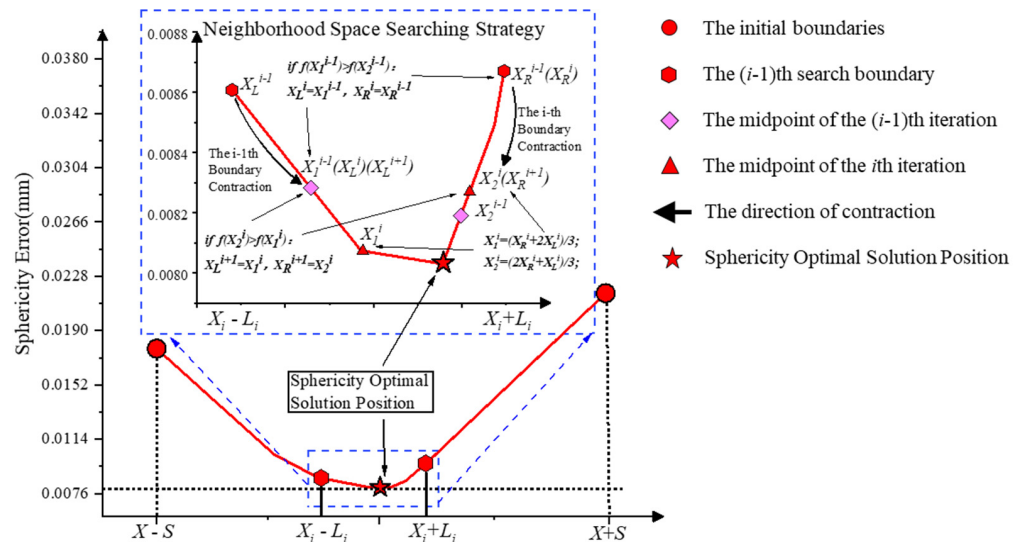
Figure 6. Schematic diagram of the search principle in a one-dimensional space.

2.5. Algorithm Flow

2.5.1. Initialization

Firstly, the population and the global temperature of the simulated annealing are initialized, and the initial least square spherical center (x_0, y_0, z_0) and least square sphericity error S_0 are solved based on the least square solution. The following is the approach for solving the least squares sphericity error S_0 and the least squares sphere center O^{LS} based on the least squares criterion. According to the coordinate dataset of the measure-

ment points, $\mathbf{p}_i = [x_i, y_i, z_i]^T, i = (1, 2, \ldots, N)$, establish the equation set $\mathbf{Ax} = \mathbf{b}$, where $\mathbf{A} = [\mathbf{p}_1, \mathbf{p}_2, \ldots, \mathbf{p}_N, \mathbf{I}]^T \in \mathbf{R}^{m \times n}$, $\mathbf{b} = [\|\mathbf{p}_1\|_2^2, \|\mathbf{p}_2\|_2^2, \ldots, \|\mathbf{p}_N\|_2^2]^T$, and $\mathbf{I} = [1, 1, \ldots, 1]^T$. By solving the equation set based on the least square solution, the coordinates of the sphere center O^{LS} (x_0, y_0, z_0) and the least square sphericity S_0 are obtained. Then, the initial population of the algorithm can be generated in the ranges of $[x_0 - S_0, x_0 + S_0], [y_0 - S_0, y_0 + S_0]$, and $[z_0 - S_0, z_0 + S_0]$, denoted as X.

2.5.2. Mutation

The mutation strategy is an important part of the DE algorithm. A suitable mutation strategy can promote the convergence of the DE algorithm to the global optimal solution. This algorithm adopts the DE/current-to-best/1/bin strategy, which uses the elite solution to guide the mutation of the existing solutions to approach the optimal one. This mutation strategy is shown in Equation (2).

$$V_i^{t+1} = X_i^t + F \cdot \left(X_{best}^t - X_i^t \right) + F \cdot \left(X_{k1}^t - X_{k2}^t \right) \tag{2}$$

where V_i^{t+1} is the *i*-th element of the vectors of mutation in the (*t* + 1)th generation; *F* is the scaling factor and a random number in (0, 0.5); X_{best}^t is the optimal solution in the *t*-th generation; X_i^t is the *i*-th element among the target vectors of the *t*-th generation; and X_{k1}^t, X_{k2}^t is the random point ($k_1 \neq k_2$).

2.5.3. Lévy Flight Based on Simulated Annealing Strategy

A Lévy flight perturbed population based on simulated annealing is introduced to enhance the diversity of the local solution space distribution. This strategy enables individuals to explore the global solution space with occasionally long trajectories and short random movements. During the exploration process of the population individuals, their corresponding local solution spaces also move within the solution space. The formula for the Lévy flight in this paper is given by $s = u/|v|^{1/\beta}$, where $u \sim N(0, \sigma^2)$, $v \sim N(0, 1)$, and $\sigma = \left\{ \frac{\Gamma(1+\beta) \sin(\pi\beta/2)}{\beta\Gamma((1+\beta)/2) \cdot 2^{\beta/2}} \right\}^{1/\beta}$.

The steps of the Lévy flight based on the simulated annealing strategy are as follows:

Step 1: Set an initial temperature T to a sufficiently high value.

Step 2: Consider the original solution of the individuals as S_1 and the new solution after Lévy flight perturbation as S_2. Calculate the difference d$f = f(S_2) - f(S_1)$ for each individual in the population, where f represents the object function.

Step 3: If d$f < 0$, accept the new solution S_2.

Step 4: If d$f \geq 0$, generate a random number R uniformly distributed in the interval (0, 1) and calculate the acceptance probability $\exp(-\mathrm{d}f/T)$ for S_2. If $\exp(-\mathrm{d}f/T) > R$, accept S_2 as the new solution; otherwise, keep the solution unchanged as S_1.

Step 5: Reduce the global temperature by setting $T = q \times T$, where $q < 1$.

As the DE algorithm progresses through iterations, the global temperature gradually decreases, resulting in a reduced probability of accepting inferior solutions. When the temperature reaches a certain threshold, the search process terminates.

2.5.4. Adaptive Local Enhancement

For a comprehensive understanding of the adaptive local enhancement process, please consult Section 2.4. Figure 5 illustrates the process of local enhancement.

Once the local solution space's search range is determined, a local optimal solution would be searched within the local solution spaces using the computational geometric method mentioned earlier. Following a greedy strategy, individuals move to the position of the local solution space's optimal solution if it is superior to their current position; otherwise, they remain at their initial positions. Then, an enhanced population is generated due to the local enhancement process, denoted as V.

2.5.5. Crossover and Selection

By mixing the new population *V* and the initial population *X* with a certain probability, a new population *U* is generated. Compare each individual in the populations *U* and *X*, and retain the ones with smaller sphericity errors for the next iteration.

The loop is ended until the conditions of convergence are satisfied, and the global optimal solution by the minimum zone criterion for evaluating the sphericity error is obtained.

3. Results

3.1. Verification with Datasets in the Literature

Due to the limited availability of publicly accessible datasets in the field of sphericity error research, current research papers often refer to the same set of publicly available spherical datasets for comparative analyses. Notably, the four datasets [15,16,31,33] used in the experiments of this section have been widely cited in numerous high-quality publications in the field of sphericity error research. As a result, these datasets hold considerable authority. By conducting experiments using these four datasets, we can effectively compare our approach with the leading algorithms in the field of sphericity error evaluation under identical experimental conditions. This reasoning highlights one of the main reasons for selecting these four datasets for experimentation in our study.

The experiments were conducted under identical conditions. The number of populations (*N*) was set to 30, the local enhancement parameter (*n*) was set to 12, the initial temperature (*T*) was set to 100, the annealing rate (*q*) was set to 0.9, and the temperature threshold was set to 0.001. Using the aforementioned settings, each dataset was independently calculated ten times. The mean and standard deviation of the results were calculated and compared with the results obtained using state-of-the-art algorithms.

Dataset 1, obtained from reference [34], comprises 100 randomly generated coordinate points within two concentric spheres with radii of 10.0 and 9.0. The data distribution is illustrated in Figure 7, where the sphericity error is determined as 1.0 based on five data points from the inner and outer spheres. The sphericity error of dataset 1 has been validated in several studies [21,34], and the algorithm's accuracy in this paper was initially assessed using dataset 1.

Ten sets of replication experiments were performed for dataset 1. The mean experimental result is 1.00000000000003 mm, with a standard deviation of 2.0×10^{-14} mm. Figure 8 displays one convergence curve from the ten experiments. Table 1 presents a comparison with the results reported in the literature.
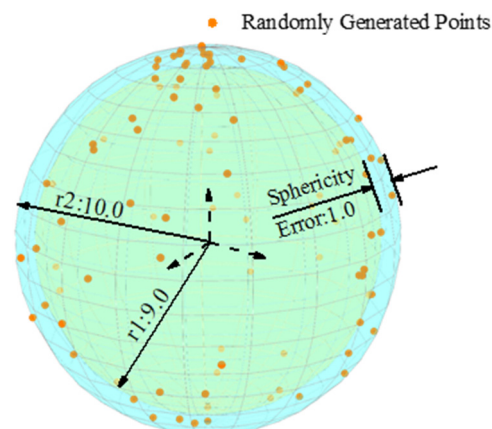
Figure 7. The distribution of dataset 1.
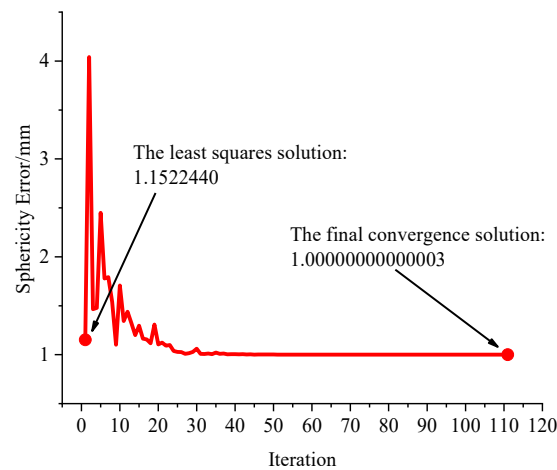
Figure 8. Algorithm optimization process (corresponding experiments based on dataset 1).

Table 1. Comparison with results based on dataset 1 in the literature (rounding is as given in the respective papers; units: mm).

Algorithm	Spherical Center Coordinate (X, Y, Z)	Sphericity Error
Least squares	$(-0.01913, 0.08935, 0.01762)$	1.15224
[34]	$(0.00000, 0.00000, 0.00000)$	1.00000
[21]	$(0.00000000, 0.00000000, 0.00000000)$	1.00000000
Ours	$(-5.3 \times 10^{-14}, 0.1 \times 10^{-14}, 1.6 \times 10^{-14})$	1.00000000000003

The number of zeros after the decimal points represents the precision provided in the original data from the cited references.

Dataset 2, consisting of 384 coordinate points, is provided in reference [16]. The 384 coordinate points were obtained through real spherical sampling using the birdcage method and were evenly distributed along 12 lines on the sphere. Figure 9 illustrates the distribution of dataset 2. The reference provides the optimal solution as 0.015385 mm. Ten sets of replication experiments were conducted for dataset 2. Table 2 presents the results of the ten experiments, with a mean experimental result of 0.01538487054930 mm and a standard deviation of 3.0×10^{-14} mm.

Figure 10 displays one convergence curve from the ten experiments. The least square solution obtained by our algorithm is 0.01639862 mm, and the final convergence solution is 0.01538487054931 mm. Table 3 presents a comparison with the results reported in the literature.

Figure 9. The distribution of dataset 2.
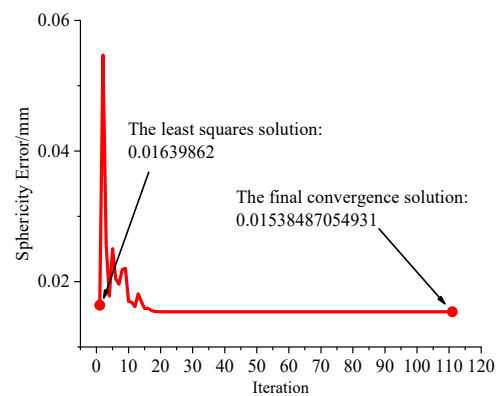
Figure 10. Algorithm optimization process(corresponding experiments based on dataset 2).

Table 2. Results of ten experiments based on dataset 2 (units: mm).

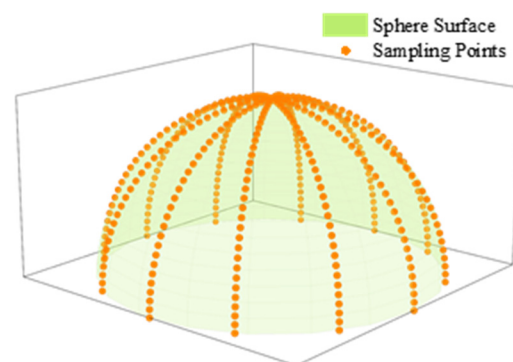| Experiment	1	2	3	4
Sphericity Error	0.01538487054931	0.01538487054927	0.01538487054934	0.01538487054926
Experiment	**6**	**7**	**8**	**9**
Sphericity Error	0.01538487054928	0.01538487054930	0.01538487054935	0.01538487054926
Experiment	**5**	**10**	—	—
Sphericity Error	0.01538487054929	0.01538487054932	—	—

Table 3. Comparison with results based on dataset 2 in the literature (rounding is as given in the respective papers; units: mm).

Algorithm	Spherical Center Coordinate (X, Y, Z)	Sphericity Error
Least squares	(−0.0001146, −0.0002871, 0.0078932)	0.01639862
[35]	(−0.0011426, 0.0000027, 0.0107779)	0.0154077
[16]	(0.000179, −0.000332, 0.011747)	0.015385
Ours	(0.0002125983629424, −0.0003506987099171, 0.01174819302036)	0.01538487054931

Dataset 3, consisting of 25 coordinate points, is provided in reference [36]. Figure 11 illustrates the distribution of dataset 3, with the coordinate points uniformly distributed on the sphere. Ten sets of replication experiments were conducted for dataset 3. Table 4 presents the results of the ten experiments, with a mean experimental result of 3.33251761616355 mm and a standard deviation of 0.8×10^{-14} mm.

Figure 12 displays a convergence curve from one of the ten experiments. The least square solution obtained by our algorithm is 3.735706 mm, and the final converged solution is 3.33251761616355 mm. Table 5 presents a comparison with the results reported in the literature.

Figure 11. The distribution of dataset 3.
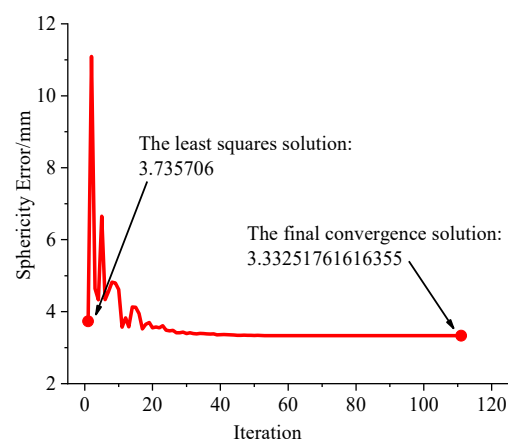
Figure 12. Algorithm optimization process (corresponding experiments based on dataset 3).

Table 4. Results of ten experiments based on dataset 3 (units: mm).

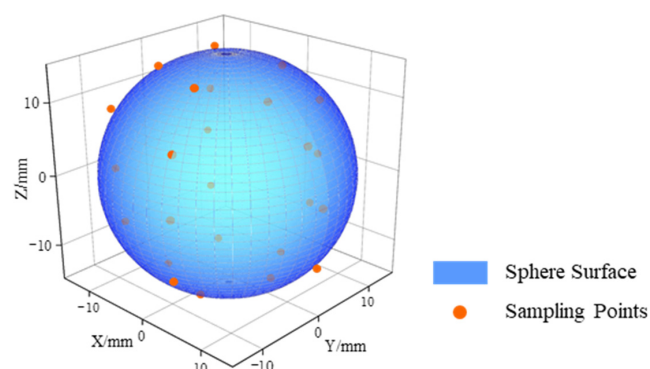| Experiment	1	2	3	4
Sphericity Error	3.33251761616355	3.33251761616354	3.33251761616355	3.33251761616355
Experiment	**5**	**6**	**7**	**8**
Sphericity Error	3.33251761616357	3.33251761616355	3.33251761616356	3.33251761616356
Experiment	**9**	**10**	—	—
Sphericity Error	3.33251761616355	3.33251761616355	—	—

Table 5. Comparison with results based on dataset 3 in the literature (rounding is as given in the respective papers; units: mm).

Algorithm	Spherical Center Coordinate (X, Y, Z)	Sphericity Error
Least squares	(−0.2545316, −0.6600826, 0.0380931)	3.735706
[27]	(−0.388729, −0.355488, −0.299887)	3.332518
[37]	(−0.38873, −0.355488, 0.299888)	3.33252
[26]	(−0.412356, −0.335014, −0.326140)	3.351375
[36]	(−0.38872967, −0.35548811, −0.29988752)	3.33251813257
[35]	(−0.3887296, −0.3554883, −0.2998876)	3.33251762
Ours	(−0.38872964944657, −0.35548834466725, −0.29988759232766)	3.33251761616355

Dataset 4, consisting of 50 coordinate points, is provided in reference [15]. Figure 13 illustrates the distribution of dataset 4, with the coordinate points randomly distributed on the sphere. Ten sets of replication experiments were conducted for dataset 4. Table 6 presents the results of the ten experiments, with a mean experimental result of 0.00766019493788 mm and a standard deviation of 0.2×10^{-14} mm.
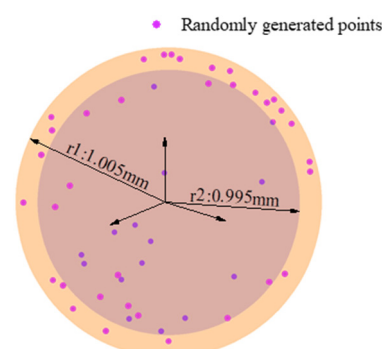
Figure 13. The distribution of dataset 4.

Table 6. Results of ten experiments based on dataset 4 (units: mm).

Experiment	1	2	3	4
Sphericity Error	0.00766019493785	0.00766019493791	0.00766019493791	0.00766019493788
Experiment	**6**	**7**	**8**	**9**
Sphericity Error	0.00766019493789	0.00766019493787	0.00766019493788	0.00766019493784
Experiment	**5**	**10**	—	—
Sphericity Error	0.00766019493787	0.00766019493786	—	—

Figure 14 displays a convergence curve from one of the ten experiments. The least square solution obtained by our algorithm is 0.008486342 mm, and the final converged solution is 0.00766019493785 mm. Table 7 presents a comparison with the results reported in the literature.
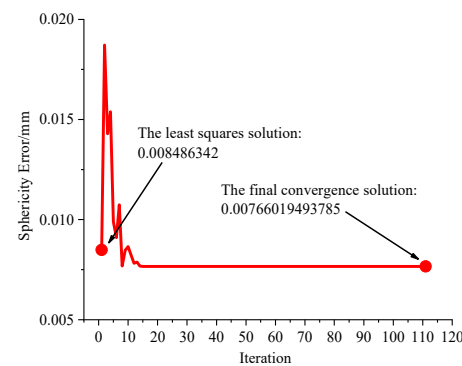
Figure 14. Algorithm optimization process (corresponding experiments based on dataset 4).

Table 7. Comparison with results based on dataset 4 in the literature (rounding is as given in the respective papers; units: mm).

| Algorithm	Spherical Center Coordinate (X, Y, Z)	Sphericity Error
Least squares	(0.0008555, −0.0003732, 0.0007853)	0.00848634
[26]	(0.000993, 0.000024, 0.000058)	0.007928
[28]	(0.002495, −0.000097, 0.000479)	0.007660
[10]	(0.002504156298, −0.000096126920, 0.000481529278)	0.007660194938
Ours	(0.00250415629838, −0.00009612691940, 0.00048152927799)	0.00766019493788

3.2. Simulated Experiments

To further assess the algorithm's accuracy, we employed the methodology described in reference [34] to generate simulated data, creating four distinct datasets. Initially, two concentric spherical surfaces, S_1 and S_2, were established with radii r_{s1} and r_{s2}, where $r_{s1} = r_{s2} + e$, and e represents the simulated spherical error.

The points on these concentric spheres were identified as control points, with ten control points generated on each inner and outer sphere. Utilizing Formula (3), by randomly generating values for θ and ϕ, we generated 100 random sampling points within the concentric sphere, culminating in a dataset comprising 120 simulated sampling points. The 20 control points on both the inner and outer spheres effectively constrained the spherical error of the simulated dataset to the difference in the radii between the inner and outer spheres. Table 8 provides comprehensive information of the spherical error, center coordinate, radii, and the number of simulated sampling points for each of the four datasets. Additionally, Figure 15 visually portrays the data distribution of these four simulated datasets.

$$X = R \cdot \cos(\theta) \cdot \sin(\phi), \quad Y = R \cdot \sin(\theta) \cdot \cos(\phi), \quad Z = R \cdot \cos(\phi) \tag{3}$$
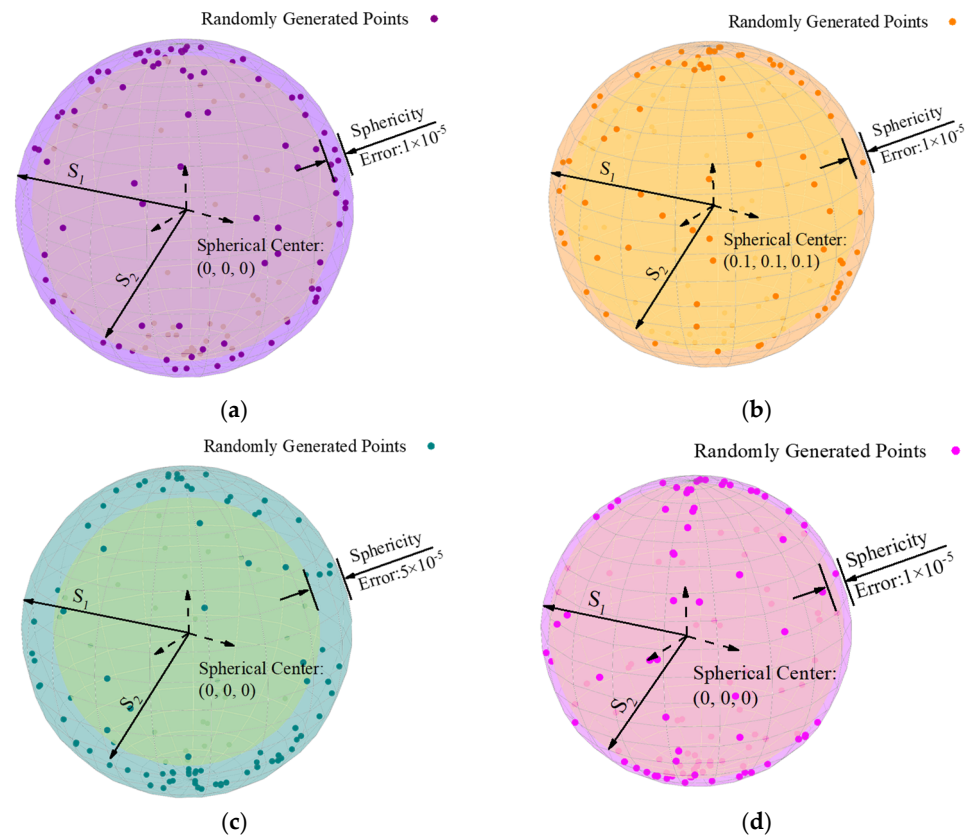
Figure 15. The distribution of simulated datasets. (**a**) Simulated dataset A; (**b**) simulated dataset B; (**c**) simulated dataset C; (**d**) simulated dataset D.

Table 8. Detailed information on the simulated datasets (units: mm).

Simulation Dataset	Spherical Center Coordinate (X, Y, Z)	Sphericity Error	Radius	Number of Coordinates
A	(0, 0, 0)	0.00001	10	120
B	(0.1, 0.1, 0.1)	0.00001	10	120
C	(0, 0, 0)	0.00005	10	120
D	(0, 0, 0)	0.00001	20	120

We conducted ten experiments for each dataset, showcasing the optimal estimates and standard deviations in Table 9. Furthermore, detailed simulated data are provided in Appendix B, Tables A2–A5. Table 9 shows that the algorithm's solutions for spherical error exhibit a deviation within the magnitude of 10^{-14} mm from the ideal spherical error. Moreover, the standard deviation of the results from ten experiments also lies within the magnitude of 10^{-14} mm. The results attest to the algorithm's successful identification of the ideal sphere center and spherical error.

Table 9. Experimental results based on simulated datasets (units: mm).

Simulation Dataset	Spherical Center Coordinate (X, Y, Z)	Sphericity Error	Standard Deviation of Results	Deviation from the Ideal Sphericity Error
A	$(6.3 \times 10^{-16}, -1.5 \times 10^{-15}, -2.8 \times 10^{-15})$	0.00001000000001	0.2×10^{-14}	1×10^{-14}
B	(0.100000000000001, 0.099999999999994, 0.100000000000000)	0.00001000000009	1.0×10^{-14}	9×10^{-14}
C	$(-3.5 \times 10^{-15}, -3.9 \times 10^{-15}, -1.6 \times 10^{-15})$	0.00005000000009	1.8×10^{-14}	9×10^{-14}
D	$(5.8 \times 10^{-14}, -3.7 \times 10^{-14}, -6.1 \times 10^{-14})$	0.00001000000005	0.9×10^{-14}	5×10^{-14}

3.3. Ablation Experiment

From the perspective of the algorithmic framework, this algorithm is based on the differential evolution algorithm, thus sharing evident similarities with traditional single-objective search algorithms. The algorithm is specifically designed to address the distribution characteristics of the sphericity error. It proposes that the resolution of the sphericity error can be treated as a unimodal function in the local solution space. Subsequently, the local enhancement method for solving this unimodal function is synergistically integrated with the differential evolution algorithm, demonstrating higher precision and robustness.

To delve into the pivotal aspects of the algorithm in this paper, we conducted ablation experiments, employing the same parameter configuration outlined in Section 3.1. We designated the algorithm with the removal of local enhancement steps as algorithm A and designated the algorithm retaining these steps as algorithm B. Subsequently, ten experiments were performed for each algorithm, with the standard deviation of the results computed. The experimental findings are documented in Table 10, from which it is evident that removing local enhancement methods significantly diminishes the algorithm's robustness, reducing the standard deviation from a magnitude of 10^{-14} mm to a magnitude of $10^{-2} \sim 10^{-7}$ mm. This experiment's results substantiate the favorable outcome achieved by amalgamating the proposed local enhancement method and differential evolution algorithm in this paper.

Table 10. Ablation experiment results (units: mm).

Dataset	Algorithm	Mean Value of Results	Standard Deviation of Results
1	A	1.00057719429339	1.7×10^{-3}
	B	1.00000000000003	2.0×10^{-14}
2	A	0.01539504919669	7.6×10^{-6}
	B	0.01538487054931	3.0×10^{-14}
3	A	3.39553011862261	9.5×10^{-2}
	B	3.33251761616355	0.8×10^{-14}
4	A	0.00766080588045	5.5×10^{-7}
	B	0.00766019493788	0.2×10^{-14}

3.4. Experiments with Datasets Obtained from CMM

To assess the proposed method's practicality, we measured a metal hemispherical shell resonator, as depicted in Figure 16b. The measurements were carried out in a controlled environment, as shown in Figure 16a, using a Hexagon CMM.

(**a**)　　　　(**b**)
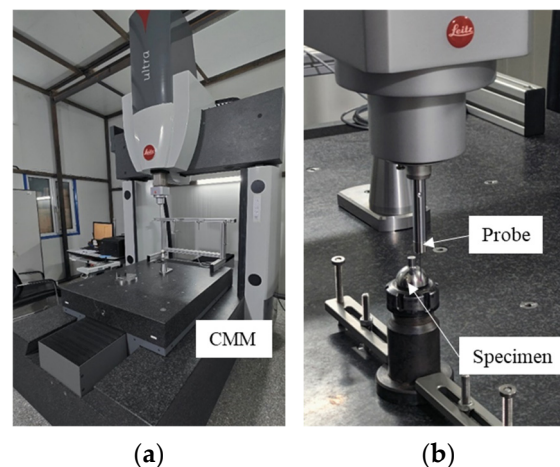
Figure 16. Measurement of a metal hemispherical shell resonator surface with a Hexagon CMM. (**a**) The Hexagon CMM and environment. (**b**) A metal hemispherical shell resonator sample was used for the spherical surface measurement.

For the measurement of the specimen, we selected five cross-sections on the surface. As detailed in Table A1, one hundred and thirty measurement points were taken. The iterative process convergence, reconstruction model of the dataset, and evaluation results are presented in Figures 17 and 18.
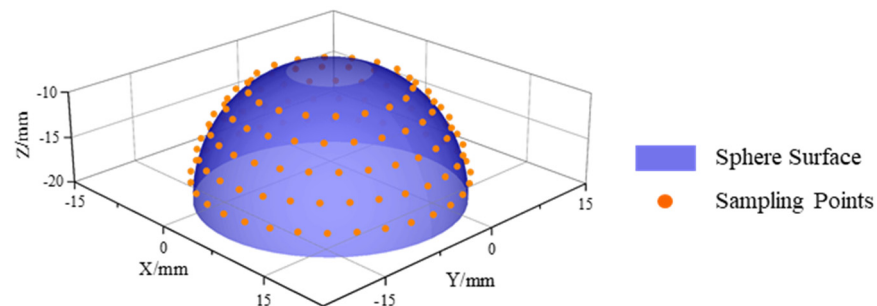
Figure 17. The dataset distribution.
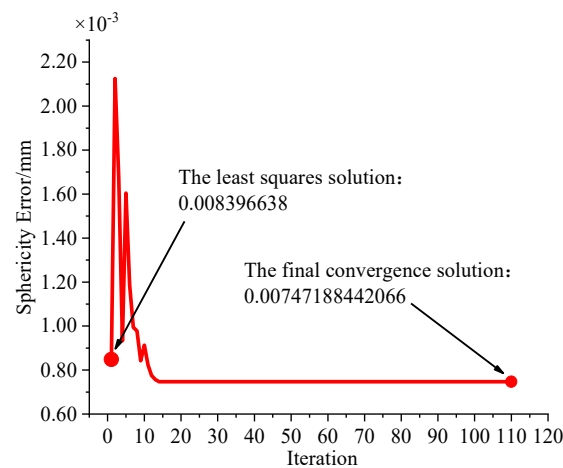
Figure 18. Algorithm optimization process.

Ten replication experiments were conducted for the measurement data. The sphericity error obtained by the CMM is 0.008396638 mm. The results of these ten experiments are presented in Table 11, indicating a mean result of 0.00747188442066 mm, with a standard deviation of 2.3×10^{-14} mm. The spherical center obtained by our algorithm is (0.00218039158405 mm, -0.00226432610011 mm, -23.9943439405 mm). Our algorithm demonstrated an 11% improvement in accuracy compared to the CMM result.

Table 11. Results of ten experiments based on measurement data (units: mm).

Experiment	1	2	3	4
Sphericity Error	0.00747188442066	0.00747188442072	0.00747188442067	0.00747188442064
Experiment	**6**	**7**	**8**	**9**
Sphericity Error	0.00747188442067	0.00747188442066	0.00747188442064	0.00747188442065
Experiment	**5**	**10**	—	—
Sphericity Error	0.00747188442065	0.00747188442064	—	—

4. Discussion

Evaluating the sphericity error based on the minimum zone criterion is an indispensable and challenging task in metrology. Thus, this study aims to achieve a high-precision evaluation of spherical contour sampling data. Consequently, we conducted an in-depth

investigation into the spatial distribution characteristics of the sphericity error. We propose treating the local space of the sphericity error as a unimodal function and utilizing computational geometry methods to obtain high-precision solutions for the local space. Subsequently, combined with the advantages of heuristic algorithms in searching the global space, we successfully achieved exact solutions for sphericity errors.

To validate the efficacy of the proposed approach, we conducted experiments using datasets that are widely cited in the realm of spherical error research, which are featured in four high-level scholarly papers. The experimental results demonstrate a significant improvement in precision, surpassing the existing achievements in the field of spherical error research by several orders of magnitude. Meanwhile, the uncertainty of the algorithm's solution reaches 10^{-14} orders of magnitude, which far exceeds that of the traditional heuristic algorithm. Furthermore, when processing the distribution of data with specific sphericity or dealing with a large number of data points, the global optimal solution can be searched out accurately using the proposed algorithm, which shows stronger robustness.

Subsequently, we conducted ablation experiments on the four datasets, as mentioned earlier. The experimental results show that, after removing the local enhancement method, the algorithm's standard deviation decreases from the order of 10^{-14} mm to the order of $10^{-2} \sim 10^{-7}$ mm. The ablation experiments demonstrate the effectiveness of the proposed local enhancement method in this paper.

Finally, we apply the algorithm to evaluate the sphericity errors of the hemispherical shell resonator and obtain its sphericity error of 0.00747188442066 mm with a standard deviation of 2.3×10^{-14} mm for ten experiments. Compared to the results obtained from the CMM, this algorithm can improve the accuracy of sphericity error evaluation by approximately 10%.

In this study, each member of the population in the DE algorithm is considered the center point for partitioning local solution spaces. During each iteration of the algorithm, computational geometric techniques are employed to solve for these individual local solution spaces. This approach has yielded outstanding precision in evaluating sphericity errors. However, it has also resulted in an algorithmic time complexity of $O(n^4)$, leading to elevated time costs for each evaluation. Furthermore, we conducted assessments of the average time required for each evaluation. Under the specified parameter settings, completing a single evaluation takes approximately 300 s. Compared to the time costs of 0.1 to 1 s in existing studies, the average time cost of our algorithm has increased several-fold. It must be acknowledged that this algorithm is not suitable for components with spherical geometry that require large-scale production and have relatively low precision requirements, such as ball bearings. In these contexts, the speed of the sphericity error assessment takes precedence over precision. However, for crucial spherical components in the entire realm of research that necessitate only one or two ultra-high precision devices, such as the ball bearings in astronomical telescopes and the electrostatic rotor in Gravity Probe B, the precision and reliability of the sphericity error assessment outweighs speed. Nevertheless, pursuing high speed and precision remains a common goal across all research domains. Therefore, reducing time costs while maintaining the existing precision level is a critical direction for future research improvements.

In summary, this study proposes an algorithm that is aimed at the high-precision evaluation of sphericity errors and that is capable of performing a highly accurate evaluation of sphericity errors. However, to achieve this high precision in sphericity error evaluation, the algorithm has made certain sacrifices in terms of the time cost. This method provides practical tools and techniques for applying ultra-precision spheres in precision engineering. It introduces new perspectives for sphericity error evaluation based on the minimum zone criterion.

Author Contributions: Conceptualization, D.Z. and J.C.; methodology, D.Z.; software, D.Z.; validation, J.C.; formal analysis, D.Z.; investigation, D.Z. and J.C.; resources, J.C., Z.W. and Y.S.; data curation, D.Z.; writing—original draft preparation, D.Z.; writing—review and editing, D.Z.; visual-

Conflicts of Interest: The authors declare that they have no known competing financial interests or personal relationships that could have appeared to influence the work reported in this paper.

Appendix A

Table A1. CMM raw coordinate indication point dataset from a hemispherical shell resonator measurement (units: mm).

No.	X	Y	Z	No.	X	Y	Z
1	8.296414	−3.02143	−11.3267	66	11.61279	5.831947	−15.6435
2	6.763515	−5.67803	−11.3267	67	12.64508	2.993801	−15.6456
3	4.413842	−7.64931	−11.3266	68	12.99436	0.00061	−15.6446
4	1.53153	−8.6978	−11.3264	69	14.36486	0.00079	−18.3304
5	−1.53198	−8.69712	−11.3262	70	14.05059	2.984275	−18.3304
6	−4.41293	−7.6497	−11.3271	71	13.12312	5.840188	−18.3305
7	−6.76176	−5.67733	−11.3264	72	11.62104	8.44174	−18.3301
8	−8.2954	−3.02146	−11.3276	73	9.610385	10.67402	−18.33
9	−8.82762	0.00175	−11.3272	74	7.180646	12.43983	−18.33
10	−8.29549	3.019205	−11.3266	75	4.436134	13.66083	−18.3294
11	−6.76226	5.675262	−11.3273	76	1.499609	14.28478	−18.3294
12	−4.41211	7.645938	−11.3277	77	−1.50034	14.28458	−18.3299
13	−1.53142	8.694617	−11.3278	78	−4.43637	13.66036	−18.3297
14	1.53211	8.694537	−11.3271	79	−7.17943	12.43851	−18.33
15	4.413092	7.645988	−11.3269	80	−9.60919	10.673	−18.3294
16	6.763165	5.674052	−11.3267	81	−11.6198	8.44048	−18.3295
17	8.296184	3.017535	−11.3274	82	−13.1219	5.839438	−18.3305
18	8.828784	0.00144	−11.3275	83	−14.0492	2.983165	−18.3305
19	11.12424	0.0013	−13.2813	84	−14.3622	0.00134	−18.3307
20	10.71211	2.999729	−13.2816	85	−14.0472	−2.98888	−18.3309
21	9.505538	5.779181	−13.2803	86	−13.1193	−5.84373	−18.331
22	7.592488	8.12935	−13.2799	87	−11.6175	−8.44454	−18.3309
23	5.115596	9.876324	−13.2799	88	−9.60736	−10.6763	−18.3306
24	2.260611	10.89058	−13.2814	89	−7.17731	−12.4413	−18.3302
25	−0.75887	11.09661	−13.2814	90	−4.43455	−13.6626	−18.3298
26	−3.72318	10.48024	−13.2821	91	−1.49886	−14.287	−18.33
27	−6.41267	9.08655	−13.2818	92	1.500999	−14.2875	−18.3296
28	−8.62704	7.018315	−13.2813	93	4.437544	−13.6644	−18.3289
29	−10.2019	4.429719	−13.2817	94	7.181086	−12.4437	−18.3295
30	−11.0187	1.511798	−13.2827	95	9.611795	−10.6784	−18.3291
31	−11.0178	−1.51657	−13.2831	96	11.62196	−8.44553	−18.3291
32	−10.2016	−4.43394	−13.2835	97	13.12441	−5.84411	−18.33
33	−8.62646	−7.02263	−13.2815	98	14.05164	−2.98806	−18.33
34	−6.41128	−9.08998	−13.2814	99	14.90208	−2.96403	−21.2295
35	−3.72154	−10.4842	−13.2812	100	14.03837	−5.81562	−21.2292
36	−0.75777	−11.0995	−13.2808	101	12.63434	−8.44279	−21.2289
37	2.261661	−10.8914	−13.2782	102	10.74393	−10.7462	−21.2288
38	5.116226	−9.87919	−13.2798	103	8.43965	−12.6363	−21.2285
39	7.592868	−8.13236	−13.2797	104	5.8119	−14.04	−21.2286
40	9.505198	−5.78223	−13.2807	105	2.961514	−14.9037	−21.2287
41	10.71221	−3.00317	−13.2805	106	−0.00016	−15.1941	−21.2291

Table A1. *Cont.*

No.	X	Y	Z	No.	X	Y	Z
42	12.64529	−2.99836	−15.6442	107	−2.96109	−14.9016	−21.229
43	11.61302	−5.83438	−15.6435	108	−5.81005	−14.0377	−21.2287
44	9.954915	−8.35568	−15.6437	109	−8.43761	−12.633	−21.2283
45	7.759662	−10.4272	−15.6439	110	−10.7396	−10.7434	−21.229
46	5.14489	−11.9356	−15.6438	111	−12.6302	−8.44041	−21.2291
47	2.254347	−12.8003	−15.6441	112	−14.0335	−5.81371	−21.2291
48	−0.75498	−12.9743	−15.6445	113	−14.8978	−2.96381	−21.2286
49	−3.72379	−12.4499	−15.6451	114	−15.1907	−0.00053	−21.2288
50	−6.49358	−11.2552	−15.6455	115	−14.9	2.961734	−21.2291
51	−8.91403	−9.45329	−15.6456	116	−14.036	5.81165	−21.2281
52	−10.8542	−7.14139	−15.6459	117	−12.6318	8.43835	−21.2283
53	−12.2073	−4.44475	−15.6464	118	−10.741	10.74128	−21.2287
54	−12.9032	−1.50946	−15.647	119	−8.43702	12.63058	−21.2273
55	−12.9038	1.506108	−15.6464	120	−5.81015	14.0345	−21.2297
56	−12.2085	4.442633	−15.6461	121	−2.9605	14.89967	−21.229
57	−10.8544	7.138399	−15.6462	122	0.00035	15.19031	−21.2285
58	−8.91463	9.450499	−15.6466	123	2.962754	14.8987	−21.2293
59	−6.49321	11.25221	−15.6457	124	5.81229	14.03412	−21.2292
60	−3.72336	12.44723	−15.6456	125	8.43856	12.63031	−21.2276
61	−0.75426	12.97149	−15.6459	126	10.74231	10.73945	−21.2293
62	2.254877	12.79544	−15.6441	127	12.63195	8.4362	−21.2295
63	5.14524	11.93096	−15.6447	128	14.03555	5.80935	−21.2291
64	7.760032	10.42313	−15.6465	129	14.89984	2.960004	−21.229
65	9.956695	8.350528	−15.6449	130	15.19234	0.00022	−21.229

Appendix B

Table A2. Simulation dataset A's coordinate data (units: mm).

No.	X	Y	Z	No.	X	Y	Z
1	2.70716589312049	5.50739356847015	7.89557274104917	61	−2.89280574054528	−3.65641016545042	8.84661176098279
2	−1.15214718780568	−9.20081371548616	3.74402430584425	62	−1.51828118667085	−9.13434218820972	−3.77606589087291
3	−1.01772769992569	−1.84485104912249	9.77552546524520	63	2.24430605422733	−4.05526495095270	−8.86103883157432
4	1.09745748886757	8.99030141206831	4.23912436513771	64	1.00655478403967	2.74990194311456	9.56164599503323
5	−1.28865793782677	−2.14712961492406	9.68138493151514	65	−5.91008390550214	6.65426786156021	4.55980568303232
6	2.23712088095506	−5.64280260263515	7.94695444739222	66	1.05649986536444	3.12247361232877	−9.44108128748343
7	0.96389378689230	9.38875252004527	−3.30491072270252	67	7.85501071612662	2.19242740865312	−5.78724691162584
8	0.09516036830667	0.57085048124596	−9.98324191519372	68	−7.39966754477964	−4.84965141456539	4.66109444057282
9	3.85822591335003	4.61648956587795	−7.98762771847785	69	1.09631832016297	−7.49379191536427	−6.53003590114144
10	−1.06721159538523	1.93885104125363	−9.75203135750703	70	3.53745810772145	−1.78161148450475	−9.18217909565151
11	6.26235696234287	−7.59196187568609	1.77341482860745	71	6.76213768840946	−0.59511144741485	7.34298594770830
12	−2.62499745458919	9.43001171406783	2.04554819936948	72	−7.89611121553721	−3.79056887081821	−4.82525144178618
13	0.29152155597613	8.30981199131132	5.55536918545053	73	−3.45995327527011	−1.48232328353041	−9.26452594664461
14	0.20630522606167	2.26036506127748	9.73900572541429	74	−0.44629221645521	−7.21658669463085	−6.90809564438316
15	2.99706563681856	−2.10102303257860	−9.30609523486725	75	0.28520194202245	0.22255761270425	−9.99346401882636
16	9.43834225665788	−2.59374462609833	2.04704082943856	76	−7.97689476851546	2.82284926180381	5.32924080069324
17	−1.60616749126634	1.85271355326272	−9.69472740038624	77	7.27215932101236	−5.15558676418842	4.53163160673812
18	−7.53700381107871	−6.54949836084845	−0.54573054674074	78	7.56765130979587	−1.13414408241597	6.43773397992703
19	9.99010525044084	0.16115167185843	0.41461566648064	79	9.10595015430749	−1.99275838613616	3.62086572061669
20	3.07794368595563	8.16192817794968	4.88971779299321	80	−1.65318551090508	−8.64678692963512	4.74342379395656
21	−8.88138219754910	3.81449533619221	2.56334286460520	81	−2.16028979995984	2.19462186324215	9.51403989099589
22	−1.50528492091493	6.14981163076181	7.74041825385070	82	3.71214714273865	1.38035475101959	9.18230164358843
23	−2.63300837329504	2.66539640573202	−9.27162121150142	83	−2.81583122618287	1.25258183256518	−9.51326201418868
24	8.56581407890788	−4.96012947251450	−1.42269021052671	84	0.25318226559820	−3.54288213674587	−9.34794068182515
25	1.82718891044369	−7.94962037867871	−5.78490312181898	85	9.50959469247850	0.37431656375598	3.07042275507506
26	8.24289514570036	−0.72547048296934	−5.61502108758284	86	−0.30358937469407	−0.37790575801959	−9.98825311874762
27	−7.70092292049896	5.21634534357503	3.67226461861028	87	6.57243761907439	−4.87188526868866	5.75047796586977
28	7.12707805126894	3.01062110905472	6.33569700257251	88	−6.01482923502479	5.09978824190112	6.14931759713210
29	−0.58999065777537	0.82156378009547	9.94872075767712	89	−5.38098973200806	−0.36572287988244	8.42088488112053
30	−2.56716043333088	1.39056147508962	9.56431299758929	90	9.64669012283484	−2.63319562276727	0.08860297026600
31	8.22189230883354	−2.82653115285224	−4.94078328448101	91	8.33083101659233	0.34658097412821	−5.52061770906743
32	5.61203365939748	−4.28243254741348	−7.08278544660527	92	1.16667377294868	−5.98585551084573	7.92518310069517
33	−8.30864658564425	−2.91133711744228	4.74241852182297	93	5.09725538078174	−8.20583203528779	2.58502319927636
34	0.66411528936322	−9.27973866238164	−3.66680749056059	94	−7.94577182052644	−0.15895145001070	−6.06955829228184
35	5.59555808812651	4.52368413040483	−6.94450142639838	95	−2.81033726124221	−0.34145895649012	−9.59090915571642
36	4.31821867358096	2.98193413994706	−8.51241352713467	96	−8.84178799766724	−1.30105332857164	−4.48666162729917
37	−7.27229290635095	−0.94799136393752	−6.79817079521441	97	−5.13240086305896	−2.53115221949677	−8.20072497861750
38	1.76614778493561	−2.67317591762393	9.47285569085848	98	−3.26949290444136	−7.24375242567628	−6.06947007104547
39	8.90488220398493	3.82356465101649	−2.46648591450760	99	−4.21044225736679	−0.91801641519192	9.02383533011225
40	−1.34216364461793	0.19580721969637	9.90759556340661	100	0.97207348091252	1.35811285724233	−9.85954941070868
41	−2.14413833249205	6.54013975411457	−7.25461521613138	101	9.97467105975975	−0.62134089971315	0.34633679834256

Table A2. *Cont.*

No.	X	Y	Z	No.	X	Y	Z
42	−0.14641530136290	0.00329534577709	−9.99893401071181	102	3.07164278927927	−7.79824967120529	−5.45458638585138
43	9.33663475800817	−2.26252230212020	2.77638143223137	103	4.21424090461527	4.13157893765339	−8.07281448962633
44	8.60615347616399	3.25778487780142	3.91419979493624	104	−8.20954862620217	2.49260305036918	5.13715697784912
45	0.92038470926800	−8.23220713076379	5.60211794144169	105	−6.05646784946783	3.33339673520736	7.22549856527915
46	0.19039170935725	−0.09559877282060	9.99773260503988	106	9.29084809507047	1.34542356946677	3.44530959845342
47	4.63041699171134	8.84538152765776	−0.56450038527465	107	3.10106100490886	9.50614519379827	0.12969193913494
48	4.90940621164029	6.17221598580318	6.14829582098568	108	8.25810929801433	−2.84241087768132	4.87077201262455
49	−1.35601812982457	2.67900851431207	−9.53856388088540	109	4.82089142825648	−1.24432507720403	8.67241820026406
50	0.10697680515944	0.16104416983599	9.99813641836490	110	8.08804152765836	−4.99592166582711	−3.10234592604136
51	0.54543741944347	−2.74352703380253	9.60081306146551	111	0.29229983657336	0.54727416058684	9.98074000592601
52	−5.88145323430974	−3.42609324921417	7.32601584952949	112	2.35365295075906	1.64164975916963	−9.57942345351573
53	1.98373588866636	2.69419177896352	−9.42371065887968	113	0.04198489879216	0.07803540541192	−9.99961698811101
54	−5.11946144416484	0.77570060507926	8.55793924257076	114	6.31161433326479	0.52599244332027	−7.73867005704883
55	−1.61607689980290	5.50777647454611	8.18857444960706	115	5.53492638583934	−8.32813270602568	−0.08363931052334
56	−6.05720577992347	−7.77957883368181	1.66986302157556	116	−1.94264324774318	−1.18582495429703	9.73756059512558
57	1.04302816178437	−3.27035836333418	9.39239093167803	117	−2.81371560108729	1.33773054919186	9.50229259300673
58	2.81296261497125	−0.15442235185868	−9.59497317966677	118	6.37164802179989	0.02784080933777	−7.70723405788024
59	0.75873469126528	−0.27199953420838	−9.96747399905116	119	−9.21326646969875	−0.10005215523293	3.88660655643943
60	−0.28319142384936	−4.90514063534900	−8.70974146028489	120	6.25059255805694	−7.80083536598516	0.27782060448905

Table A3. Simulation dataset B's coordinate data (units: mm).

No.	X	Y	Z	No.	X	Y	Z
1	1.34866310044556	−3.42964434197735	9.37267364430173	61	−6.03813011492763	−7.76545546035172	−0.57679931500770
2	6.28762586455096	−5.81093158895213	5.27438015487295	62	−8.37817918397411	−3.42734922369600	4.05958662316408
3	0.58398271936605	1.85955926550385	9.93207905167647	63	0.52233695646431	3.25269396882814	9.58062372503846
4	−6.79335005575682	−6.71332209489238	2.56179219875112	64	−2.09026691610244	3.65529455010974	9.18639845896016
5	4.55446618682185	0.04056169255594	−8.85288769493223	65	−9.81740328667709	−0.73694309391516	1.07199737940335
6	3.79620842970985	−7.53588616139182	5.39445802461468	66	0.15445504692498	0.12627148991291	10.09982417701270
7	−9.83674200746524	1.06675729653396	0.67151129024692	67	0.50101334310798	0.22752854129214	10.09115232442710
8	−6.61532798308528	−3.65557088498325	−6.28750106664630	68	9.74076804798352	0.73231251158527	2.67987835617744
9	−7.17985071352343	1.34974236352629	6.84106883141816	69	0.10312758013623	−9.70002495549256	2.08989240315612
10	7.85510652795512	−5.94733723625945	1.91329825334280	70	−8.82575264163078	3.18405414406231	3.38931694468529
11	−5.08174827571728	8.28746885629698	2.57282723147979	71	6.95710495543139	−1.95896587491257	−6.88146426353406
12	−4.17476966096297	−1.38927722347042	9.01674947115353	72	8.14147891565005	−0.62754515133087	−5.79960757253585
13	7.39523184514386	−1.64735595814567	−6.51258975851859	73	4.73021563852859	−8.34043159678178	−2.60562618722498
14	1.75791425129314	9.35998423612448	−3.29177150326352	74	0.14885226061423	−2.55233387947583	9.74172384433377
15	9.53037413100502	2.96783323871382	−1.58629448613162	75	0.24123084998983	3.35834622385500	−9.35321815255340
16	1.06836312520230	−9.74081253052169	1.59019545332327	76	−9.17601252417074	1.72155553651928	−3.26545594466951
17	−1.35961492444953	8.85325919098271	−4.50977555465138	77	1.24207417896070	−9.83319802271571	0.26564340074693
18	−2.54886701298226	−1.16362897579127	−9.45964508557108	78	3.95019276558823	−0.43913982247625	−9.11333454632599
19	8.34553977625825	−3.82986427250573	−3.97030706242059	79	1.01943786643079	−8.65011678471033	4.85290752422392
20	−9.06726678345875	2.76301281032927	−2.87819871193943	80	−1.37244324949174	−0.44407560653978	−9.77602856563217
21	−2.70120696204215	7.93041862738558	5.65318756342506	81	−3.01546757149110	−8.62853994942254	3.85585826136877
22	0.40484779625699	−2.40089122619986	9.77743521432033	82	0.89864570124804	2.04062555358302	−9.67733289275361
23	8.34419183403123	0.27817441678260	−5.55699346407081	83	1.04201185554798	9.23553399933964	−3.85660415833079
24	−9.00214396824030	2.94261718779047	3.11174899152034	84	7.94146024657417	−1.16315196293439	−5.97586605514242
25	4.33215924680972	8.94616766180038	−1.85811718467211	85	−0.10384830725595	−2.04850736620220	9.86434844241350
26	−8.59344894888064	4.59342781058663	2.15743814789502	86	−2.22329768993876	−1.15500863645621	9.74507341073813
27	−4.96057364591641	8.47029337115301	2.18057426683214	87	2.45491666352924	5.78849624684043	−7.78007284896142
28	−3.22871530473500	−0.06432575276105	−9.32829802706838	88	−5.68774904080877	1.63805685551568	−7.90852031663867
29	−0.41110364489163	−2.67992872798330	9.69222845496206	89	5.59040668462846	5.33875629313861	6.61236943075913
30	−4.68903899887497	7.25889644785651	5.18088675419929	90	0.43818779380963	8.97196368206258	−4.50152918880770
31	9.41291069990909	0.66348567366363	−3.49891347368823	91	2.03348649684924	−0.05004258783391	9.91015953014887
32	0.94818881511365	−6.65575236452663	−7.22396030057950	92	0.42240670799693	1.11071074115523	−9.84357670621854
33	−1.67590490013474	−9.35455804128937	2.83086859879816	93	8.59284720462050	−4.75746548879856	−1.96799907697002
34	−4.16989182916701	7.86070284138004	4.74107785938835	94	−7.75645964799996	2.11408393073890	5.94974621604521
35	3.25227913344670	−6.58739533739249	6.83364607621087	95	−6.57387031107005	7.25023913010277	2.18173076947982
36	2.79496959426060	8.19466092640749	5.31668384631082	96	0.26916625306042	0.25589604520815	10.09736113827280
37	8.93129544156749	−0.38889049269008	−4.56575556136091	97	−3.46440861622413	−5.00614749907289	7.92447755025208
38	3.18101226342569	−1.52942164932200	−9.27296903448642	98	7.75906351118220	−1.28779877499083	6.37796001575860
39	7.04242471712940	2.41100805551266	−6.71631389000110	99	−9.50971105265897	−2.34766336070543	−1.18936949313789
40	−4.84619856008049	8.30681576997033	−2.76067603756258	100	−7.84248425564078	4.56684661186731	4.21877363426257
41	−4.85601964526380	−5.43098753280862	6.79672419090749	101	0.54593631811652	0.03153202952144	−9.88981746265683
42	−8.12420949331687	4.47991361320555	−3.53027084236835	102	0.11657353763262	0.57993270390538	10.08847086418930
43	8.47190154368879	−5.08576199441910	−1.63716848889158	103	4.28376953167379	7.70072695757926	5.07243383167886
44	−1.49064300895679	9.97071885482340	−0.09724232947774	104	−1.84255095146451	0.60951826428967	−9.69627313630365
45	2.60842772256343	3.60002146556946	−8.92539971975359	105	1.71428502293959	5.13723178893266	8.58649396213649
46	−3.83790555020136	−9.07413849353980	0.67279290583042	106	7.51446382502934	−6.59902638575811	−0.28577127558744
47	−0.02360421418595	−8.77097210922236	−4.51418638304886	107	−7.04181353646521	5.45351438097204	4.60937233528599
48	−9.33039977030179	−1.14575492021222	3.18475178506461	108	6.12487358526707	3.77291668319337	−6.98594726658885
49	6.95165799200241	−6.22900417099728	3.70536794271800	109	4.53745658457334	0.85209846515610	9.02991192334709
50	3.21824046995196	7.57046071349043	5.97101496312303	110	−1.12776216963448	−1.82149594347224	9.83655759421291
51	−4.22634034562955	4.97567752136581	7.68357899479138	111	−3.63485132545628	−2.96062615963476	8.65691411102701
52	3.13366413705399	4.08476978070495	−8.55555571092744	112	0.15207573590189	−9.50293289978279	−2.68947447382110
53	−8.92065921311551	−4.00273826814577	−1.23991189847763	113	−5.67454541558127	−5.35441490987012	6.17486513203551
54	−1.27823634621782	5.65258577982205	8.30177913980271	114	2.46258257926635	9.58063747653475	2.22976234541775
55	3.42467444593053	−5.91207099422011	−7.16648072928937	115	4.15121428825438	0.20895663027339	9.24198564645230
56	4.42158568224405	1.50997493058889	−8.80707402406929	116	5.01626077364017	4.64750359467024	7.52635676060415
57	−2.52027470099493	5.12888276079702	−8.13677720163141	117	7.14553350213879	7.11330722565636	1.18355485513316
58	−7.66578663482778	−4.23480394172058	−4.47188682700721	118	−3.65814281845417	6.93857742396894	−6.15382574716082
59	2.10766041854642	7.07201098260663	−6.78189486210131	119	6.91217239125644	0.22870336010611	7.41968187538919
60	3.62675332328140	4.24915024848378	8.48729188985141	120	−4.21831012911677	−0.73580262084969	−8.88074058906206

Table A4. Simulation dataset C's coordinate data (units: mm).

No.	X	Y	Z	No.	X	Y	Z
1	5.95996262889717	−2.53087159418200	−7.62062810900662	61	−3.51246706823379	−9.34182505861613	0.62737974656962
2	−9.85107314551679	−1.30444876074718	−1.12023703431943	62	4.50473221625104	−6.05203499045717	6.56362954642608
3	−0.42562009583607	1.60551591345338	−9.86110403170941	63	3.94183536430941	7.27924518817052	5.61030276751094
4	7.15248741603897	−5.79696049895956	−3.90354930806442	64	1.10547040857635	7.49865115145544	−6.52295453806957
5	−8.79810084568203	4.72470932722656	0.52086306669802	65	0.28826524595727	5.08233406156181	−8.60741492035918
6	2.28942095507661	−3.32448286731950	−9.14911828294701	66	−9.33209675238265	−1.88494780973294	−3.05933742850091
7	−0.23648593817369	0.53665373133653	−9.98283913404341	67	1.24171798290095	−4.99923896512844	−8.57125197473802
8	1.20968561171675	2.77318121266279	9.53133145254380	68	−1.22194940877846	−1.79255182349007	−9.76189481363779
9	5.93420067374265	−3.08518708773780	−7.43423399317568	69	−2.33658986292916	0.40834911563586	9.71465342116742
10	−1.83054232077633	−0.60978790824329	−9.81211687345779	70	−2.50791452160276	9.32268233296792	2.60746212216540
11	−6.42127372632781	−5.52810017703587	−5.31108701348930	71	7.43197381777530	−4.30470977913549	−5.12213226028162
12	1.19848917351491	6.75231597828767	−7.27810776457924	72	4.23679718803602	6.88574958202849	5.88530467085766
13	−0.42583197337906	6.13395610992908	7.88628269665551	73	−3.35333670814301	9.24977931999824	−1.78798670354391
14	6.57382699453694	−4.69870339578870	5.89130064077983	74	9.71840199364162	−1.82443538824880	−1.49161565565493
15	−0.67205602261595	3.15416628864922	9.46571213695177	75	−8.19193551995640	1.67782531605284	−5.48429567206496
16	0.27155434387497	0.27118450797139	−9.99266903431794	76	0.40140787070271	−1.33286253492707	−9.90266817867122
17	0.25308083307023	−0.04010002834001	−9.99676658135817	77	4.53726053260564	0.94151974265130	−8.86154770747293
18	−1.17788531771628	−0.24510239526266	−9.92740700432568	78	1.61516813350064	6.96306357529998	−6.99336339363929
19	7.06536392207105	2.21510220623939	6.72121934542273	79	9.25819273048234	−1.16503736461130	−3.59564896620229
20	−5.31128165470666	1.05688392418140	−8.40678477561395	80	−6.28584646497884	−2.28309780959583	−7.43482055476037
21	−2.11065116617518	−4.16503976045407	−8.84295772138813	81	−0.19178974586890	0.09521260975715	−9.99775058306743
22	2.15886526922128	−8.54779992582657	4.71964413912382	82	8.50066661341672	−2.40179219786582	4.68722320418105
23	5.88541066182448	−1.27357658674910	−7.98376490192677	83	−6.41886291974595	−6.69020924991784	3.74696167129575
24	−1.85389822982494	1.07643711617595	−9.76753200091694	84	−2.17639276771440	−9.70204539665303	−1.06518995694937
25	7.27117064778413	6.83385042030464	−0.65533759053807	85	−1.24902071442348	9.91581613986789	0.31446178943944
26	−5.71954621436550	4.10020977591656	7.10462799391528	86	4.00910113808578	9.08862361957577	1.15069225193287
27	5.08401851378667	−0.02960672336012	8.61117654902158	87	−3.79323507426728	−8.78984680325001	−2.88972600375784
28	−0.26443730535060	−0.03053847330009	9.99647246809361	88	7.37207044548441	6.54996548881943	1.65869014847620
29	9.07084930001875	−3.86540812389358	−1.66690047914021	89	4.37274176835174	−0.22139490848028	−8.99057566771884
30	2.86805392843574	−5.57345457408119	−7.79174779263483	90	−9.20458184798071	−2.74927686394480	−2.77804077503713
31	−3.95616029511580	−1.76938209469346	−9.01216304362207	91	3.84083333935019	−1.51569516697420	−9.10772569965450
32	2.36818512714166	6.74525808213302	6.99239242962638	92	−2.59334387393980	−0.26239126724716	9.65431239809196
33	6.08354542163128	−5.08223798323700	−6.09601467195711	93	0.78419338417084	−3.04987739990699	−9.49124240726619
34	8.51756401769817	−2.59707326287336	−4.55050613105236	94	9.00676579747105	3.26512839593949	2.86659322301019
35	−0.00150849137714	0.00176617463060	10.00001997397680	95	−2.92902631777872	3.69839622648143	−8.81720186526334
36	−8.87466688583470	−4.10078607200066	2.10329295561852	96	0.98664286932946	−8.90409024626217	−4.44345701534720
37	−2.03549057294796	6.11701773694590	7.64453217229997	97	7.86678077709667	−6.13458879926826	−0.69374280606344
38	8.53705944581464	4.35922961278074	−2.84898800509080	98	−1.15725800979753	2.63128895976783	9.57794718658249
39	−9.11528166103595	4.06506417766708	−0.62279561377970	99	−0.14579857774420	−0.21121056560729	−9.99673047090975
40	−0.58102184165576	9.61081481618440	−2.70102749001126	100	−1.25580657367142	−0.10475745442277	−9.92030984831879
41	0.35321082337023	8.17644980500951	−5.74645650108488	101	7.01763907424743	−0.69202363480080	−7.09047566216930
42	5.67461369627328	−4.99499972058684	−6.54595569871264	102	−0.65388617986357	2.57232761613757	−9.64137918690304
43	2.79553200396705	9.41125152721134	1.90102278229729	103	6.04398530035203	7.30171439964982	−3.18676666787718
44	−5.76116096867094	8.16829018858550	0.29803366260499	104	−5.39008334649265	−2.99099011441192	7.87410240772113
45	0.81231109499248	−1.76130591724466	9.81010561518831	105	6.00375943305308	4.59441140239776	−6.54573283811845
46	6.78433265308395	−2.49420282986743	−6.91032129106041	106	9.04407550772326	1.53304034917810	3.98189176899673
47	1.86420286158789	9.16431100680814	3.54120762753932	107	−4.97523299033828	−2.57612725498324	−8.28317226619606
48	0.46310293309069	9.73696812348966	2.23106840315640	108	2.27648031534053	2.92945614899788	−9.28636253779010
49	1.88555388454493	−2.55997340072303	−9.48113694822441	109	1.72083737286512	6.52616757239851	−7.37887901737959
50	−6.56595707040798	−4.98992000387135	−5.65595158951884	110	−2.78810706129170	−1.41914467735619	−9.49804109497103
51	0.60930958004152	0.31233873760694	−9.97656149520066	111	6.13684273879640	−3.07613391500331	−7.27163312280270
52	4.81820410624501	−5.81186464235642	−6.55805905523815	112	−2.65206520094611	8.05998897351177	5.29183351617852
53	−6.92416985159192	−6.38950809436772	−3.35122442675302	113	7.65293149411519	−6.40840365705949	0.60418841047588
54	−4.01794200780133	−5.59775753776835	7.24715479138558	114	0.56486545100115	3.08894380518371	−9.49422379061154
55	−9.79487189140082	−1.04454957796796	−1.72335488571771	115	−1.04130724007516	−1.53503208605850	−9.82651289771900
56	2.52865790796924	−5.60942584080151	−7.88293580244636	116	−4.23561751907541	0.83262679515559	9.02037958499682
57	−7.46647640711460	5.76777831438991	−3.31443258802386	117	−1.36156873609851	3.96780352924388	9.07759140577493
58	1.60575217539826	−4.85236205171849	8.59514801850770	118	3.01460153226631	−2.37159102989348	9.23514540246705
59	0.45562100548285	−1.85585394689852	−9.81574065321849	119	−9.08538775384136	3.96172735036234	1.32686651808811
60	0.60898677943533	4.94763038814187	−8.66894807615183	120	−1.13534715705872	−5.15041230845435	−8.49618460850138

Table A5. Simulation dataset D's coordinate data (units: mm).

No.	X	Y	Z	No.	X	Y	Z
1	1.01827397046852	−16.58223949132140	−10.89363718109050	61	6.06383239458524	18.62029549152800	4.72943319369740
2	−13.34805033351610	−7.65151186352272	−12.51207364609940	62	−17.49268728408530	−9.37509388839011	−0.74855543825462
3	−10.85895498342310	−7.82787277400729	−14.63262159123280	63	−2.95050821623490	13.32859826311390	−14.5866933276464
4	−7.82688204692040	18.45532417824060	−0.39679573595063	64	−1.46204046352872	−0.81330288421109	20.01798450174830
5	10.30900200779320	−10.09332954684140	−13.75181254401260	65	0.61694120175509	14.37587094279790	−13.8975848364538
6	−14.42304045809420	−2.42937674159383	−13.39815874421950	66	7.22220058167940	−1.51110523690333	18.71931724681080
7	−8.70626533118663	15.72064958615080	8.95694047270114	67	−6.38849699666628	0.99329051206819	−18.7971296197525
8	−9.46047435993298	−4.33118464803028	17.09888036481630	68	−11.1092678813575	2.70467302295429	−16.2575098727216
9	−8.55574557041805	−3.61813827146386	17.74238975917280	69	19.17624788295150	3.18008400778801	5.25848048259532
10	−4.47575358740484	12.02394048345430	15.49097535747460	70	0.57400332298236	3.18735409862370	−19.6545834053648
11	1.18157843626710	−19.84688771532510	−0.87583530092755	71	−8.84843005167697	−10.9152758645158	−13.9921756195152
12	12.72462790755350	−1.79655645813156	−15.29552638807290	72	−3.00177343917124	0.17099678521819	−19.6578936374463
13	−7.35643350554795	6.18067041315640	−17.43359765133640	73	−12.7896452288276	10.09334240088980	−11.4754176273606
14	1.16280745257179	−0.72078948835909	20.05487057595220	74	17.90839450288090	−3.54156658135182	8.44268197993650
15	−0.20813104833264	14.58208632995030	13.89037089100960	75	2.96106596202016	16.5298129237656	11.13973450479910
16	18.25367735889010	7.11608071063607	4.70636837294161	76	−13.1465617890625	7.62914121276286	−12.8553476744905
17	11.49696314639260	−15.44165803526220	5.44473018996573	77	−8.74646065591191	11.6322946576240	13.83850132902650
18	−2.16392469089001	0.83039496171992	−19.75803535584460	78	2.79968153573403	19.3874358147267	−4.45045599529497

Table A5. *Cont.*

No.	X	Y	Z	No.	X	Y	Z
19	1.68355633012895	1.88620054874559	19.95703920979820	79	−1.48496404285976	0.59388529302004	20.0309817973941
20	19.64394830582460	1.21531889197613	4.19761492813433	80	1.86825643905109	−4.75766614049884	−19.2203666266285
21	3.91144426005375	3.79462348595604	19.38270338799840	81	−0.83656074379294	−0.96746618861219	−19.8495205433453
22	18.55485035335030	6.58707162584348	−4.06370550974975	82	−5.49492644661469	10.73418866681580	−15.8878462959520
23	−14.97456160827260	−1.11066147552205	−12.98786432268080	83	−3.80093220200770	3.13541687496168	−19.2796042424803
24	3.44585801675839	9.94215773899642	−16.98618053201200	84	−15.5880823519049	9.40106327444076	−8.10819659849956
25	−6.09016836774572	−2.68963529620687	−18.71222460492920	85	−18.2576547031961	1.12895640488274	7.97006084712438
26	−13.04807418539690	−12.54947668265840	8.29261704609541	86	10.49536571786190	13.79659705098480	−10.1146838692175
27	2.09518671398468	−1.27224569517222	19.95286733485780	87	8.80543241338193	−17.6458457320953	−2.94971131041900
28	4.75455189488812	16.99344821169060	−9.54088810370740	88	9.25865041278559	−1.10120558793086	−17.6391233771429
29	19.47523087979740	0.94602374245893	−4.78723537598508	89	−17.8505562022870	4.57435019426862	−7.49985287327967
30	−9.71939483968772	1.80999356221063	17.43942205559590	90	−10.2523954188985	3.66547938695731	−16.6366468132108
31	4.23624746745487	−16.37834724788520	−10.45251291712490	91	11.56502410835130	−11.1667931585712	−11.8001152889516
32	1.94122091567610	13.98457288292260	14.37685396574550	92	−11.4073320118934	−13.9933247567537	−8.20420717407658
33	−5.03249637040109	−6.51268030718956	18.26397713914980	93	10.68001801215560	−15.4856240086703	−6.61951623427540
34	−1.15179970349694	6.29548586292803	−18.87496615486860	94	5.90864697584834	−17.3422835277526	7.97570731093767
35	1.64898027593959	9.77027856807626	−17.33808038472760	95	0.46667722969903	20.02206521434100	−1.62541336683918
36	−2.05629356124958	9.48209963488476	17.63073541917730	96	−10.9615942160357	4.47191929407413	16.17879762919220
37	3.85411379778398	1.69588783533586	−19.47958316498940	97	2.28810905920513	−3.44111150716674	−19.4620277927884
38	14.15697204354040	−13.90269899135140	−2.41522522348013	98	16.8840174126687	10.08724836843570	−4.20718583643146
39	−0.20426992002611	0.59263673296207	20.09161674097680	99	−11.2759557549732	−5.18433912532622	15.6776614308102
40	−2.52544544260464	4.92288722155417	−19.13141167663400	100	−5.82328105745985	13.7707838301110	13.4425890803288
41	−4.81520178654368	−2.58331884937223	19.30002516048620	101	1.81833972088083	−11.2270398427722	16.4934610087666
42	−0.89198658551585	−10.55279166077970	−16.79776256611030	102	−11.3169550065854	15.5247657046385	−5.53294932892596
43	−11.52970092308250	−12.92085836386540	−9.65743574420629	103	18.49717636238000	5.51582670251050	−5.57565972709238
44	−4.30687911070277	19.03743999244430	−4.58540004091944	104	−17.5915674679496	−9.22534652387289	−0.11610300895466
45	−1.79046902193470	−14.74656897912440	−13.16672147081700	105	15.51142832766370	−4.53322523123523	11.97156707998060
46	−0.82428299505741	−1.48334775795102	−19.81580019684510	106	1.80602316138195	16.57927332615510	11.30372090674270
47	17.97958117110970	6.26641754870141	6.60353642503426	107	18.88028253243810	6.77916276141418	1.74012279350019
48	−11.55695697104530	−16.10452986112690	1.33648772641715	108	2.44185338612605	−11.5128302064991	−16.0139102367006
49	−6.51472496606937	−9.82199878493186	−15.95614003247500	109	10.96228303494210	−14.4365979646038	−8.30823285377158
50	−10.62843762891630	5.65690585856826	16.03805256053560	110	14.93418188835610	7.49990446899727	11.28877720486080
51	1.49454173751660	−2.95598487258305	−19.61588724356240	111	−2.00751746160698	−4.96094780607129	−19.1339669360993
52	6.23560828673115	4.92507746739824	−18.31393326764820	112	−19.8774126579963	−0.34144282531075	−0.74157929219974
53	18.50688544822750	7.85024987758855	−0.95855926192827	113	0.59781614332414	17.79372679846470	−9.21044241612647
54	17.03503404541520	−1.29200862828843	10.64832253787790	114	−6.72848396486137	14.21862165584770	−12.3111457743369
55	−4.99871766746520	−16.35724069453180	−10.05689590652830	115	18.40346933418050	6.73345294480625	−4.48043076869942
56	17.46517828652930	−9.81754829167634	−0.20486078186585	116	9.68390059042623	13.13011708211820	11.86285452827500
57	−12.38615898015310	5.42369983733961	14.78857190219600	117	−9.07980486558268	−2.47679609248717	−17.4809966968707
58	14.01561202466960	12.06231488177630	−7.85355051623286	118	15.53268989669770	5.56740835811171	11.58649332044970
59	−1.08752796169960	0.04350469111739	−19.86463520577670	119	−6.31395438498343	0.32145413074370	−18.8423392515690
60	17.26857507163890	9.80599181861071	3.42176555650988	120	−1.10382109828030	15.73986163459290	−12.3074793094377

References

1. Everitt, C.W.F.; Lipa, J.A.; Siddall, G.J. Precision engineering and Einstein: The Relativity Gyroscope experiment. *Precis. Eng.* **1979**, *1*, 5–11. [CrossRef]
2. Lipa, J.A.; Siddall, G.J. High precision measurement of gyro rotor sphericity. *Precis. Eng.* **1980**, *2*, 123–128. [CrossRef]
3. Stojadinovic, S.M.; Majstorovi, V.D. *An Intelligent Inspection Planning System for Prismatic Parts on CMMs*; Springer International Publishing: Cham, Switzerland, 2019.
4. Pathak, V.K.; Singh, R. A Comprehensive Review on Computational Techniques for Form Error Evaluation. *Arch. Comput. Method Eng.* **2022**, *29*, 1199–1228. [CrossRef]
5. Acko, B.; Mccarthy, M.; Haertig, F.; Buchmeister, B. Standards for testing freeform measurement capability of optical and tactile coordinate measuring machines. *Meas. Sci. Technol.* **2012**, *23*, 94013–94025. [CrossRef]
6. *ISO 1101:2017*; Geometrical Product Specifications (GPS), Geometrical Tolerancing, Tolerances of Form, Orientation, Location and Run-out. ISO: Geneva, Switzerland, 2004.
7. Cogorno, G.R. *Geometric Dimensioning and Tolerancing for Mechanical Design*; McGraw-Hill Education: New York, NY, USA, 2020.
8. Samuel, G.L.; Shunmugam, M.S. Evaluation of sphericity error from coordinate measurement data using computational geometric techniques. *Comput. Methods Appl. Mech. Eng.* **2001**, *190*, 6765–6781. [CrossRef]
9. Liu, F.; Xu, G.; Zhang, Q.; Liang, L.; Liu, D. An intersecting chord method for minimum circumscribed sphere and maximum inscribed sphere evaluations of sphericity error. *Meas. Sci. Technol.* **2015**, *26*, 115005. [CrossRef]
10. Zheng, Y. A simple unified branch-and-bound algorithm for minimum zone circularity and sphericity errors. *Meas. Sci. Technol.* **2020**, *31*, 045005. [CrossRef]
11. Fanwua, M.; Chunguang, X.U.; Haiming, L.I.; Juan, H. Sphericity evaluation using maximum inscribed sphere method. *Procedia Eng.* **2011**, *24*, 737–742. [CrossRef]
12. Meng, F.W.; Xu, C.G.; Li, H.M.; Hao, J. The Relationship between Minimum Zone Sphere and Minimum Circumscribed Sphere and Maximum Inscribed Sphere. *Appl. Mech. Mater.* **2012**, *157–158*, 658–665. [CrossRef]
13. Meng, F.W.; Xu, C.G.; Hao, J.; Xiao, D.G. Sphericity evaluation based on minimum circumscribed sphere method. *Adv. Mater. Res.* **2012**, *433*, 3146–3151. [CrossRef]
14. Fei, L.; Guanghua, X.U.; Lin, L.; Qing, Z.; Dan, L. Intersecting Chords Method in Minimum Zone Evaluation of Sphericity Deviation. *J. Mech. Eng.* **2016**, *52*, 137–143.

15. Fana, K.C.; Lee, J.C. Analysis of minimum zone sphericity error using minimum potential energy theory. *Precis. Eng.* **1999**, *23*, 65–72. [CrossRef]
16. Liu, F.; Xu, G.; Liang, L.; Zhang, Q.; Liu, D. Minimum zone evaluation of sphericity deviation based on the intersecting chord method in Cartesian coordinate system. *Precis. Eng.* **2016**, *45*, 216–229. [CrossRef]
17. Janecki, D.; Stępień, K.; Adamczak, S. Sphericity measurements by the radial method: I. Mathematical fundamentals. *Meas. Sci. Technol.* **2015**, *27*, 015005. [CrossRef]
18. Janecki, D.; Stępień, K.; Adamczak, S. Sphericity measurements by the radial method: II. Experimental verification. *Meas. Sci. Technol.* **2015**, *27*, 015006. [CrossRef]
19. Lei, X.; Gao, Z.; Duan, M.; Pan, W. Method for sphericity error evaluation using geometry optimization searching algorithm. *Precis. Eng.* **2015**, *42*, 101–112.
20. Kanada, T. Evaluation of spherical form errors—Computation of sphericity by means of minimum zone method and some examinations with using simulated data. *J. Jpn. Soc. Precis. Eng.* **1995**, *17*, 281–289. [CrossRef]
21. Huang, J.; Jiang, L.; Zheng, H.; Xie, M.; Tan, J. Evaluation of minimum zone sphericity by combining single-space contraction strategy with multi-directional adaptive search algorithm. *Precis. Eng.* **2019**, *55*, 189–216. [CrossRef]
22. Mao, J.; Zhao, M. An Approach for the Evaluation of Sphericity Error and Its Uncertainty. *Adv. Mech. Eng.* **2013**, *2013*, 67–77. [CrossRef]
23. Cha, Y.; Agrawal, A.K.; Kim, Y.; Raich, A.M. Multi-objective genetic algorithms for cost-effective distributions of actuators and sensors in large structures. *Expert Syst. Appl.* **2012**, *39*, 7822–7833. [CrossRef]
24. Cha, Y.; Kim, Y.; Raich, A.M.; Agrawal, A.K. Multi-objective optimization for actuator and sensor layouts of actively controlled 3D buildings. *J. Vib. Control* **2013**, *19*, 942–960. [CrossRef]
25. Cha, Y.J.; Raich, A.; Barroso, L.; Agrawal, A. Optimal placement of active control devices and sensors in frame structures using multi-objective genetic algorithms. *Struct. Control. Health Monit.* **2013**, *20*, 16–44. [CrossRef]
26. Cui, C.C.; Che, R.S.; Ye, D. Sphericity error evaluation using the genetic algorithm. *Opt. Precis. Eng.* **2002**, *10*, 333–339.
27. Wen, X.; Li, H.; Wang, F.; Wang, D. Sphericity error united evaluation using particle swarm optimization technique. In Proceedings of the 2009 9th International Conference on Electronic Measurement & Instruments, Beijing, China, 16–19 August 2009; IEEE: New York, NY, USA, 2009; pp. 1-156–1-161.
28. Wen, X.; Song, A. An immune evolutionary algorithm for sphericity error evaluation. *Int. J. Mach. Tools Manuf.* **2004**, *44*, 1077–1084. [CrossRef]
29. Jie, H.; Changcai, C.; Fugui, H. Sphericity error evaluation based on a modified particle swarm optimizer using dynamic inertia weight. *J. Graph.* **2012**, *33*, 99–103.
30. Yu, X.; Huang, M.; Xia, P. Sphericity Error Evaluation Based on an Improved Particle Swarm Optimization. *Comput. Syst. Appl.* **2009**, *12*, 201–203.
31. Jiang, L.; Huang, J.; Ding, X.; Chao, X. Method for spherical form error evaluation using cuckoo search algorithm. In Proceedings of the 10th International Symposium on Precision Engineering Measurements and Instrumentation (ISPEMI 2018), Kunming, China, 8–10 August 2018.
32. Xiulan, W.; Aiguo, S. An improved genetic algorithm for sphericity error evaluation. In Proceedings of the International Conference on Neural Networks and Signal Processing, 2003. Proceedings of the 2003, Nanjing, China, 14–17 December 2003; IEEE: New York, NY, USA, 2003; pp. 549–553.
33. Chen, M. Analysis of spherical form errors to coordinate measuring machine data. *JSME Int. J. Ser. C* **2002**, *45*, 647–656. [CrossRef]
34. Huang, J. An exact minimum zone solution for sphericity evaluation. *Comput.-Aided Des.* **1999**, *31*, 845–853. [CrossRef]
35. Calvo, R. Sphericity measurement through a new minimum zone algorithm with error compensation of point coordinates. *Measurement* **2019**, *138*, 291–304. [CrossRef]
36. Wang, M.; Cheraghi, S.H.; Masud, A.S. Sphericity error evaluation: Theoretical derivation and algorithm development. *IIE Trans.* **2001**, *33*, 281–292. [CrossRef]
37. Cui, C.; Fan, W.; Huang, F.; Li, B. An Iterative Method for Minimum Zone Sphericity Error Evaluation. *Iran. J. Mater. Sci. Eng.* **2011**, *1*, 367.